Impact of Chronic and Massive Resuspension Mechanisms on the Microphytobenthos Dynamics in a Temperate Intertidal Mudflat

R. Savelli, Xavier Bertin, F. Orvain, Pierre Gernez, A. Dale, T. Coulombier, P. Pineau, N. Lachaussée, P. Polsenaere, C. Dupuy, et al.

JGR Biogeosciences

RESEARCH ARTICLE
10.1029/2019JG005369

Impact of Chronic and Massive Resuspension Mechanisms on the Microphytobenthos Dynamics in a Temperate Intertidal Mudflat

R. Savelli[1], X. Bertin[1], F. Orvain[2], P. Gernez[3], A. Dale[1], T. Coulombier[1], P. Pineau[1], N. Lachaussée[1], P. Polsenaere[4], C. Dupuy[1], and V. Le Fouest[1]

[1]LIttoral, ENvironnement et SociétéS (LIENSs), Université de La Rochelle, UMR 7266, CNRS-ULR, La Rochelle, France, [2]Université de Caen Basse-Normandie, UMR BOREA (MNHN, UPMC, UCBN, CNRS-7208, IRD-207), Caen, France, [3]Mer Molécules Santé (MMS) - EA 21 60, Université de Nantes, Mer Molécules Santé, Nantes, France, [4]IFREMER, Laboratoire Environnement Ressources des Pertuis Charentais (LER/PC), L'Houmeau, France

Abstract Microphytobenthos (MPB) resuspension is a key mechanism in the transfer of organic matter from productive intertidal mudflats to terrestrial and marine systems. In this study, we infer on the contribution of physical and biological factors involved in the MPB resuspension. We use a physical-biological coupled model forced by realistic meteorological and hydrodynamical forcings to simulate chronic (without any concomitant sediment resuspension) and massive (driven by bed failure) resuspension over a year. The model simulates mud surface temperature, MPB growth, and grazing by the gastropod *Peringia ulvae*. The model suggests that MPB resuspension is the highest in spring tides and at the flood beginning due to high current velocity and low water heights that promote waves-sea bottom interactions. The seasonal export of MPB biomass is the highest in spring, up to threefold higher than in summer when the export is the lowest. The simulated seasonal dynamics of MPB resuspension results from the MPB biomass concentration in the sediment, physical disturbances, and the bioturbation activity by *P. ulvae*. Annually, 43% of the simulated MPB primary production is resuspended. The MPB resuspension (60.8 g C·m^{-2}·yr^{-1}) exceeds the loss by *P. ulvae* grazing (41.1 g C·m^{-2}·yr^{-1}). The model suggests that chronic and massive resuspension events are important in the synoptic to seasonal MPB dynamics in temperate intertidal mudflats. Accounting for such processes in the carbon budget assessment in the land-ocean interface could bring new insights to our understanding of the role played by MPB in the coastal carbon cycle.

Plain Language Summary Intertidal mudflats support a high biological productivity sustained mainly by microalgae living in the sediment. Microalgae form a dense biofilm at the surface of the mud during daytime low tides and fix a high quantity of inorganic carbon into organic carbon through photosynthesis. Microalgae can be resuspended along with the sediment into the sea water during the high tides. Such a transfer is facilitated by episodic physical disturbances like waves and currents modulated by biological drivers. Our study aims to simulate with a numerical model the biologically mediated chronic and physically driven episodic massive resuspension of microalgae on an intertidal mudflat for year 2012. The model is a useful tool to disentangle and estimate the respective contribution of physical and biological factors involved in the microalgae resuspension. At the tidal scale, the resuspension of microalgae is the highest at the flood beginning and during spring tides due to higher current velocity and low water heights that promote waves-sea bottom interactions and sediment erosion. In 2012, the simulated microalgae resuspension is the highest in spring and the lowest in summer. In the model, the seasonal dynamics of microalgae resuspension results from the microalgae biomass in the sediment, physical disturbances, and the grazers activity at the mud surface that remobilized and facilitated the microalgae resuspension, a process called bioturbation. Annually, 43% of the simulated organic carbon produced by microalgae is resuspended over the year. As microalgae sustain the food web in the mud and in the sea water, their production and resuspension are of key importance for the functioning of coastal ecosystems and the sustainability of economic activity such as shellfish farming. Moreover, estimating the export of organic carbon from the mud to the water is essential to understand the contribution of microalgae biofilms to carbon cycle of the global coastal ocean.

Key Points:
- Seventy-six percent of microphytobenthos biomass resuspended at flood beginning
- Spring massive and chronic events represent 20% and 17.5% of the annual microphytobenthos export, respectively
- Forty-three percent of annual microphytobenthos primary production is resuspended

Correspondence to:
R. Savelli,
raphael.savelli1@univ-lr.fr

Citation:
Savelli, R., Bertin, X., Orvain, F., Gernez, P., Dale, A., Coulombier, T. et al. (2019). Impact of chronic and massive resuspension mechanisms on the microphytobenthos dynamics in a temperate intertidal mudflat. *Journal of Geophysical Research: Biogeosciences*, *124*, 3752–3777. https://doi.org/10.1029/2019JG005369

Received 9 JUL 2019
Accepted 30 SEP 2019
Accepted article online 1 NOV 2019
Published online 12 DEC 2019
Corrected 10 FEB 2020

This article was corrected on 10 FEB 2020. See the end of the full text for details.

Author Contributions

Conceptualization: R. Savelli, P. Polsenaere, C. Dupuy, V. Le Fouest
Data curation: R. Savelli, X. Bertin, F. Orvain, P. Gernez, A. Dale, T. Coulombier, P. Pineau, N. Lachaussée, P. Polsenaere, C. Dupuy, V. Le Fouest
Funding Acquisition: F. Orvain, P. Polsenaere, C. Dupuy, V. Le Fouest
Methodology: R. Savelli, X. Bertin, F. Orvain, P. Gernez, T. Coulombier, P. Polsenaere, C. Dupuy, V. Le Fouest
Software: R. Savelli, V. Le Fouest
(continued)

Validation: R. Savelli, X. Bertin, P. Gernez, V. Le Fouest
Writing - Original Draft: R. Savelli, X. Bertin, P. Gernez, P. Polsenaere, C. Dupuy, V. Le Fouest
Formal Analysis: R. Savelli, X. Bertin, F. Orvain, A. Dale, T. Coulombier, V. Le Fouest
Investigation: R. Savelli, X. Bertin, P. Gernez, A. Dale, T. Coulombier, P. Pineau, N. Lachaussée, P. Polsenaere, C. Dupuy, V. Le Fouest
Project Administration: P. Polsenaere, C. Dupuy, V. Le Fouset
Resources: X. Bertin, F. Orvain, P. Gernez, T. Coulombier, P. Pineau, N. Lachaussée, P. Polsenaere, C. Dupuy, V. Le Fouest
Supervision: P. Polsenaere, C. Dupuy, V. Le Fouest
Visualization: R. Savelli, V. Le Fouest
Writing - review & editing: R. Savelli, X. Bertin, P. Gernez, P. Polsenaere, C. Dupuy, V. Le Fouest

1. Introduction

Tidal flats play a key role in the structure and functioning of coastal areas (Healy et al., 2002; Millenium Ecosystem Assessment, 2005). Benthic microalgae or microphytobenthos (MPB) living in intertidal and shallow sediments significantly contribute to the high biological production of coastal ecosystems (MacIntyre et al., 1996; Underwood & Kromkamp, 1999). MPB assemblages consist mainly of diatoms, cyanobacteria, euglenophyta, and chlorophyta, which vary with sediment properties (Underwood, 2001). In sandy, coarse and noncohesive sediments, MPB are composed by epipsammic taxa that live in close association with sediment grains (Underwood, 2001). In very fine cohesive sediments, MPB consist mainly of free motile epipelic cells that bury in the first centimeter of sediment during high tides and migrate up to the sediment surface during daytime low tides (Underwood, 2001). At the sediment surface, the MPB photosynthetic rate is driven by mud surface temperature (MST) and solar irradiance (Barranguet et al., 1998; Cartaxana et al., 2013; 2015; Perkins et al., 2010; Vieira et al., 2013). At optimal levels, they drive a high MPB primary production (PP) up to 1.9 g C m^{-2} day^{-1} (Underwood & Kromkamp, 1999). The MPB production is transferred to adjacent terrestrial and marine zones through trophic export (Carlton & Hodder, 2003; Galván et al., 2008; Jardine et al., 2015; Perissinotto et al., 2003; Saint-Béat et al., 2013) and hydrodynamics (Ubertini et al., 2012). During the rising tide, MPB cells are susceptible to be resuspended in the water column (de Jonge & van Beusekom, 1992, 1995). Therefore, in addition to the direct export to benthic food webs through grazing (Herman et al., 2000; Jardine et al., 2015; Kang et al., 2006; Lucas et al., 2001), MPB also sustain pelagic suspensive and filter feeders, such as herbivorous fishes and zooplankton, as well as wild or farmed shellfishes (Krumme et al., 2008; Leroux, 1956; Newell et al., 1989; Paulmier, 1972; Perissinotto et al., 2003).

The MPB resuspension consists of chronic resuspension of MPB cells without any concomitant sediment resuspension and of episodic massive resuspension driven by bed failure. As MPB are associated with sediment, MPB resuspension can be driven by the same hydrodynamical mechanisms that govern sediment resuspension. In intertidal mudflats, tidal currents can be strong enough to induce the resuspension of unconsolidated sediment (Mehta et al., 1989). However, only high bed shear stress (BSS) driven by waves, combined or not with tidal currents, can resuspend consolidated sediment (Bassoullet et al., 2000; French et al., 2008). Episodes of strong waves and tidal currents can therefore remobilize a sediment surface layer deeper than 1 cm (Andersen et al., 2007; Christie et al., 1999) and export a high quantity of MPB biomass to the water column, identified as massive resuspension (Mariotti & Fagherazzi, 2013). Moreover, MPB control the bed failure probability by stabilizing the sediment upper layer. The excretion of extracellular polymeric substances (EPSs) mainly by MPB, increases the sediment consolidation and its resistance to hydrodynamical disturbances by binding the sediment particles together (Austen et al., 1999; Decho, 1990; 2000; Madsen et al., 1993; Paterson, 1989; Pierre et al., 2010; 2012; Underwood & Paterson, 1993).

In conditions without any bed failure, chlorophyll pigments originating from MPB biofilms were measured in the water column and were related to the fluff layer erosion (Blanchard et al., 1997; Dupuy et al., 2014; Orvain et al., 2014; Wiltshire et al., 1998). This biogenic fluff layer is formed by the tracks, mucus, and pellets generated by grazing, crawling, and egestion of benthic deposit feeders at the sediment surface containing MPB cells and sediment grain (Le Hir et al., 2007; Willows et al., 1998). The fluff layer formed through the action of bioturbation is not bounded to the sediment bed and can be eroded more easily (Andersen, 2001; Blanchard et al., 1997; Davis, 1993; Orvain et al., 2003; Willows et al., 1998). Consequently, normal hydrodynamical conditions can promote fluff layer erosion and associated MPB more frequently. Such a process can be considered as chronic resuspension (Orvain et al., 2014).

The in situ monitoring of the MPB export from the sediment to the water column is not trivial. This is due to the highly responsive behavior of MPB when exposed to the highly variable physical (light, temperature, tide, and waves) and biological (MPB dynamics, bacteria, and grazers) conditions. Remotely sensed data of MPB cover a wide range of spatial scales (approximately from one to a few hundred meters) but their limited number of products and their limited time resolution (approximately from one to several days and 1 hr for geostationary satellites) impede our capacity to investigate the underlying processes of the retrieved state of MPB (e.g., Benyoucef et al., 2014; Brito et al., 2013; Daggers et al., 2018; Gernez et al., 2017; Méléder et al., 2018).

Physical-biological coupled modeling is a complementary tool to field and remote sensing studies to better understand physical and biogeochemical processes prevailing in these complex intertidal systems. Our

Table 1
List Abbreviations and Symbols Cited in the Text

Abbreviation	Definition
MPB	Microphytobenthos
PP	Primary production
Chl *a*	Chlorophyll *a*
C	Carbon
EPS	Extracellular polymeric substances
BSS	Bed shear stress
REF_{run}	Reference simulation in which MPB are resuspended at a constant rate
PHY_{run}	Simulation with the explicit representation of wave- and tidal-induced MPB resuspension and fluff layer erosion
Symbol	Definition
F	MPB biomass in the sediment first centimeter
S	MPB biomass in the biofilm
B	MPB biomass in the fluff layer
Z	*Peringia ulvae* biomass
γ	Mean time spent by a cell at the surface
F_{mini}	Background MPB biomass in the sediment
$\tau_{baresed}$	Critical BSS for bare sediment
$\tau_{crit_{fluff}}$	Critical BSS for fluff layer erosion
$\tau_{crit_{mass}}$	Critical BSS for massive resuspension
τ_c	Current BSS
τ_w	Wave BSS
τ_{max}	Maximal BSS combining both τ_c and τ_w
z_0	Bed roughness length
E_0	Mud erosion constant
ω	Consolidation factor by biofilm
ν	*P. ulvae* crawling rate
B_{max}	Saturation of Chl *a* concentration in the fluff layer

study aims to estimate the chronic and massive MPB resuspension and to infer on its role on the seasonal MPB dynamics over one of the largest intertidal mudflat of the French Atlantic coast, in the Bay of Marennes-Oléron. We used a physical-biological coupled model that simulated the seasonal pattern of MPB growth and grazing by gastropod deposit feeder *Peringia ulvae*. In the paper, we first describe the coupled physical-biological modeling approach. Then, we assess the role and the temporal variability of each resuspension type (chronic vs. massive) on the MPB dynamics. Finally, we discuss the importance of considering MPB resuspension to better understand the coastal food webs functioning and the seasonal exporttothe water column of organic matter mediated by MPB (Table 1).

2. Material and Methods

2.1. Study Site

The study area is the Pertuis Charentais Sea, a shallow semienclosed sea on the French Atlantic coast (Figure 1). It is characterized by a semidiurnal macrotidal regime (tidal range ~6 m at spring tides). In the southern part of the domain, the Bay of Marennes-Oléron covers 170 km^2 including 60 km^2 of intertidal mudflats. The study site (45°54′50″N, 01°05′25″W) is located in the Bay, on the Brouage mudflat (Figure 1). It is a 42-km^2 intertidal mudflat made of fine cohesive sediments (median grain size 17 μm and 85% of grains with a diameter <63 μm; Bocher et al., 2007) and characterized by a gentle slope (~1/1,000; Le Hir et al., 2000). The concentration of total suspended matter over the mudflat lies in the range 50–80 mg L^{-1} at neap tides and can reach 500 mg L^{-1} at spring tides (Kervella, 2009). North of the Brouage mudflat, the turbidity usually takes values between 4 ± 1 NTU and 12 ± 8 NTU in summer and winter, respectively (Luna-Acosta et al., 2015). South of the mudflat, it varies between 10 ± 8 NTU and 14 ± 12 NTU in summer and winter,

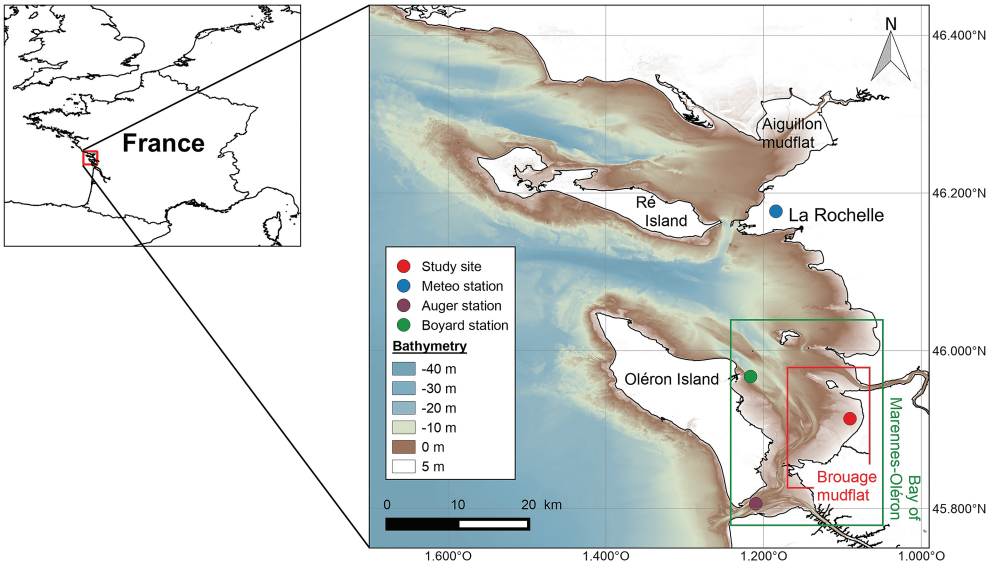

Figure 1. Bathymetric map of the Pertuis Charentais Sea (source: French marine service for hydrography and oceanography-SHOM) and location of the main intertidal mudflats. The study site and the Meteo France weather station are represented by a red and a blue full point, respectively. The two REPHY monitoring stations are represented by the purple and green full points.

respectively (Luna-Acosta et al., 2015). The highest current velocity reached at neap and spring tides is ~0.2 m s^{-1} and 0.5 m s^{-1}, respectively (Le Hir et al., 2000). On the Brouage mudflat, the wave height was measured as up to 0.7 m (Bassoullet et al., 2000). As in many mudflats along the northern European Atlantic coast, a dense biofilm of epipelic MPB develops at the surface of the mudflat at low tide and can reach up to 25 mg Chl *a* m^{-2} (Herlory et al., 2004). When resuspended by waves and tidal currents, MPB can contribute significantly to in-water Chl *a* measured in the area (from 4 to 16 mg Chl *a* m^{-3}; Guarini et al., 2004; Soletchnik et al., 1998, 2017; Struski & Bacher, 2006).

2.2. Observations

A large multiparametric data set of physical and biological measurements collected in the Pertuis Charentais Sea was used to constrain the model and to compare with the model outputs. We provide here a summary of the data used along with their respective references, within which a detailed methodology of each set of measurements can be found.

2.2.1. In Situ Data

We used 2012 atmospheric forcings to constrain the MST model and the MPB model. Atmospheric forcings consisted of hourly meteorological observations (shortwave radiations, air temperature in the shade, and relative humidity) acquired at the Meteo France weather station located near the La Rochelle airport (46°10′36″N, 1°11′3″W; data available online at https://publitheque.meteo.fr; Figure 2). They were complemented by hourly sea level atmospheric pressure and wind velocity extracted from the atmospheric reanalysis CFSR (NCEP Climate Forecast System Version 2 [CFSv2] selected hourly time series products, https://rda.ucar.edu/datasets/ds094.1) at the study site (Figure 2). Atmospheric forcings span from 1 September 2011 (03:00 UTC) to 31 December 2012 (23:00 UTC).

An acoustic Doppler current profiler mounted with a pressure transducer (ADCP; Aquadopp Profiler 2MHz, Nortek AS) was deployed on the sea bottom from 19 April 2012 (12:00 UTC) to 22 April 2012 (12:00 UTC). The ADCP data were used to compare with the water depth, the current velocity, and the wave parameters simulated by the SCHISM model and used to constrain the coupled physical-biological model. The ADCP was set to measure 1-min mean velocity profiles with a 0.1-m vertical resolution followed by 10-min continuous measurements at 2 Hz, where current velocities were averaged in a 0.5-m-thick cell. Power spectral density estimates were computed using five overlapping and hanning-windowed segments, which results in 10 degrees of freedom and a frequency resolution of 0.0196 Hz. Pressure attenuation with depth was corrected using linear wave theory. The spectral significant wave height Hm0, and the mean wave period Tm02 were computed integrating the corrected power spectral density from 0.05 to 0.44 Hz.

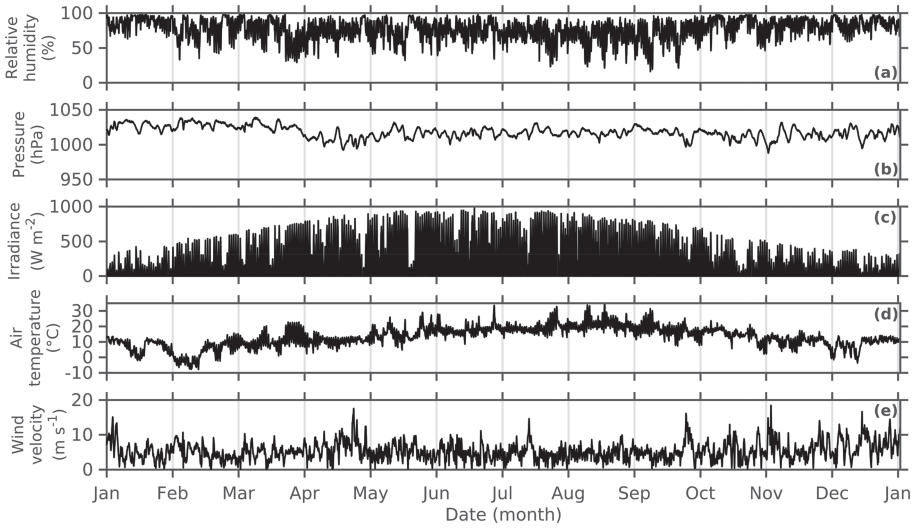

Figure 2. Time series of the 2012 (a) relative humidity, (b) atmospheric pressure above the sea, (c) global irradiance, (d) air temperature in the shade, and (e) wind velocity at the study site.

The overall consistency of the MPB compartment was assessed using both field and satellite-derived data of chlorophyll concentration. We compared the simulated resuspended MPB biomass (mg Chl *a* m^{-3}) with the in-water Chl *a* concentration (mg Chl *a* m^{-3}) measured at two sampling stations of the French Phytoplankton and Phycotoxin Monitoring Network (REPHY; Belin & Raffin, 1990; French Observation and Monitoring program for Phytoplankton and Hydrology in coastal waters, 2017) in the Pertuis Charentais Sea. The samples were collected twice a month at a subsurface depth (between 0 and 1 m) with a HYDROBIOS sampling bottle (2.5 L). The first station is the Boyard station located at the East of Oléron island (Figure 1). The second station is the Auger station located to the South of the Bay of Marennes Oléron (Figure 1; Soletchnik et al., 2017, 2018). In addition to Chl *a* concentration, we also used the phytoplankton cells taxonomic identification from the same samples, in order to differentiate the contribution of resuspended benthic species to the total microalgae cell counts. Taxonomic identification was performed at the class to species level. Class and species were associated to a full or partial benthic growth and pelagic growth form according to the classification given in Hernández Fariñas et al. (2017). Counts (number of cells per liter) were used to determine the contribution of each forms. Only Chl *a* measurements from samples in which the contribution of benthic form exceed 50% were used.

2.2.2. Remote Sensing Data

In addition to in situ REPHY data, we compared the simulated Chl *a* data with space and time-coincident cloud-free satellite data from the Medium Resolution Imaging Spectrometer on-board the polar-orbiting environmental research satellite (ENVISAT) of the European Space Agency. Medium Resolution Imaging Spectrometer has a global coverage of 3 days and a horizontal resolution of 300 m in Full-resolution mode (Rast et al., 1999). Level2 data of spectral marine reflectance were downloaded from the European Space Agency's MERCI server (https://merisfrs-merci-ds.eo.esa.int/). The Chl *a* concentration was computed using a semianalytical inversion algorithm specifically developed for coastal and inland waters (Gons, 1999; Gons et al., 2005). The algorithm used the spectral bands at 665, 705, and 775 nm, and the Chl *a* retrieval was performed in three steps.

The backscattering coefficient (b_b) was first estimated from the water reflectance (ρ_w) at 775 nm:

$$b_b(775) = \frac{1.61\rho_w(775)}{0.082 - 0.6\rho_w(775)} \quad (1)$$

Then, a near-infrared/red band ratio was used to compute the phytoplankton absorption at 665 nm:

$$a_{\text{phy}}(665) = \frac{(0.70 + b_b)\rho_w(705)}{\rho_w(665)} - 0.40 - b_b^p, \quad (2)$$

where p is a constant set to 1.02 (Gernez et al., 2017). Finally, Chl *a* concentration (mg Chl *a* m^{-3}) was obtained by dividing the phytoplankton absorption by the chlorophyll-specific absorption coefficient at 665

nm (a^*_{phy}):

$$[Chl\,a] = \frac{a_{phy}(665)}{a^*_{phy}(665)} \quad (3)$$

The value of a^*_{phy} (0.014 m^2 (mg Chl a)$^{-1}$) was set up from Gons results, which correspond to the average computed from a large variety of inland and coastal water samples. As communication with ENVISAT-1 was lost on 8 April 2012, six cloud-free high tide scene images were extracted from 4 January to 1 April 2012. Chl a concentration was estimated at the pixels corresponding to the study site (Figure 1).

2.3. The Coupled Physical-Biological Model

2.3.1. The MST Model

A mud temperature model was coupled to a two-layer biological model and run for the year 2012. The model is not horizontally resolved. Heat fluxes were simulated in a 1-cm-deep sediment layer through a set of thermodynamic equations detailed in Savelli et al. (2018). The simulated temperature of exposed mud resulted from heat exchanges between the Sun, the atmosphere, the sediment surface, from the heat conduction between mud and air, and from mud evaporation. The simulated surface (1 cm) temperature of immersed mud was set to the temperature of the overlying seawater, which resulted from thermal conduction between air and seawater, upward seawater radiation, and downward solar and atmospheric radiation. The MST simulated by the model was successfully compared to 2008 in situ 1-min data at the same study site (see Savelli et al., 2018). The differential equation was solved with a 30-s Euler-Cauchy scheme.

2.3.2. The MPB Model

The biological model explicitly represented the MPB biomass concentration in the surface biofilm compartment (S, mg Chl a m^{-2}) and in the sediment first centimeter (F, mg Chl a m^{-2}). The MPB model was developed and calibrated for epipelic diatoms. Exchanges of MPB biomass between the biofilm and the underlying sediment were ruled by a vertical MPB migration scheme according to the diurnal and tidal cycles (Guarini et al., 1998). During the daytime emersion period, the MPB cells migrated upward in the sediment from F to the S compartment until the biofilm saturation. In the biofilm, the MPB growth rate depended on the photosynthetically active radiation, the simulated MST, and the grazing pressure. The potential time spent by the MPB at the surface was calculated before each low tide by the parameter γ^* (h):

$$\gamma\ *= \left(\frac{F}{S_{max}} + 1\right) \times \gamma, \quad (4)$$

where S_{max} is the saturation value of the surface biofilm (25 mg Chl a m^{-2}) and γ is the mean time spent by a MPB cells at the surface (1 hr; Blanchard et al., 2004). The formula sets the potential duration of MPB biofilm at the sediment surface during daytime emersion periods by dividing the MPB biomass in F into fractions of biofilm (S_{max} = 25 mg Chl a m^{-2}) that spend 1 hr in average at the sediment surface. The higher is the biomass in F, the longer is γ^*. This potential time is independent of the duration of the daytime emersion periods, which can be shorter or longer. As soon as MPB exceeded their potential duration at the surface, they migrated downward from S to the F compartment. MPB migrated downward also at nightfall and during immersion if hydrodynamical conditions were calm (i.e., when $\tau_{max} < \tau_{crit_{mass}}$, see section 2.3.5). The grazing pressure was simulated through the *Peringia ulvae* biomass (Z, mg C m^{-2}) grazing on MPB at the sediment surface. The *P. ulvae* growth rate was related to the MST and the simulated MPB biomass.

The crawling activity of *P. ulvae* generates at the sediment surface a fluff layer composed by a mineral and organic matrix including MPB cells. Consequently, we introduced a new compartment that represented the dynamics of MPB biomass in the fluff layer. Such a compartment was not taken into account in Savelli et al. (2018). The fluff layer was represented by the B compartment (mg Chl a m^{-2}), supplemented by a flux of MPB biomass from the biofilm to the fluff layer:

$$\frac{dB}{dt} = \min\left[S \times \left(1 - \frac{B}{B_{max}}\right) \times vZ, \frac{S}{dt}\right], \quad (5)$$

where B_{max} is the saturation of Chl a concentration in the fluff layer. Considering a mean Chl a concentration in the sediment of 500µg Chl a g^{-1} of dry sediment and a maximal resuspended mass of sediment of 23 g of dry sediment m^{-2} (Orvain et al., 2007), B_{max} was set to 11.5 mg Chl a m^{-2}. Here, Z was expressed in density of individuals (ind m^{-2}) using the same *P. ulvae* monthly averaged individual weight estimated in Savelli et al. (2018). Therefore, the higher is the MPB biomass in the biofilm (S), the higher is the flux of MPB biomass

from the biofilm to the fluff layer. This flux was also modulated by the density of *P. ulvae* individuals (Z) and their crawling rate υ ($m^2 \cdot s^{-1} \cdot ind^{-1}$).

2.3.3. The SCHISM Modeling System

The SCHISM modeling system (Zhang et al., 2016) was used to obtain the 2012 ten-minute time series of water height (m), east-west and north-south depth-integrated velocity (m s^{-1}), significant wave height (m), mean wave period (s) and direction (°), and wave orbital velocity (m s^{-1}) used to compute the BSS and emersion-immersion periods used to constrain the physical-biological model. SCHISM fully couples several modules to simulate, for example, hydrodynamic circulation, short waves, and sediment transport and that all share the same unstructured grid and domain decomposition. In the present application, the 2DH circulation model was fully coupled with the spectral wave model Wind Wave Model II (hereafter WWM-II; Roland et al., 2012), which were implemented over the study area using an unstructured grid with a spatial resolution ranging from ~2 km along the open boundaries and ~100 m in the Bay of Marennes-Oléron. The circulation model uses the combination of an Eulerian-Lagrangian method with a semi-implicit scheme, which relaxes the Courant-Friedrichs-Lewy condition associated with the advection of momentum and allows for stable and accurate numerical results, even using large time steps. Along its open boundary, the circulation model was forced with amplitudes and phases of the 19 main tidal constituents, linearly interpolated from the regional model of Bertin et al. (2012). Over the whole domain, the circulation model was forced by wind and sea level pressure fields at 10 m above the sea surface originating from the CFSR reanalysis, with spatial resolutions of 0.20° and 0.5°, respectively. SCHISM was fully coupled with WWM-II using a radiation stress formalism (Longuet-Higgins & Stewart, 1964). WWMII simulates short wave generation and propagation by solving the wave action equation (Komen et al., 1996) using a four-step fractional method. In the present application, the source terms included wave growth and dissipation by whitecapping according to Bidlot et al. (2007), nonlinear-wave interactions computed using the Discrete Interaction Approximation of Hasselmann et al. (1985), bottom friction using the JONSWAP approach (Hasselmann et al., 1973) and depth-induced breaking using the model of Battjes and Janssen (1978). The fields were extracted at the node corresponding to the study site.

2.3.4. BSS Computation

The current BSS (τ_c, Pa) was calculated assuming a logarithmic velocity profile in the first layer above the sea bottom (Schlichting & Gersten, 2016):

$$\tau_c = \rho u_*^2, \text{ with } u_* = \frac{\kappa u(z)}{ln\left(\frac{z}{z_0}\right)}, \tag{6}$$

where u_* is the current friction velocity (m s^{-1}), ρ is the seawater density (kg m^{-3}) and κ is the Von Karman constant (0.4). z is the water height (m), and $u(z)$ is the associated depth-integrated current velocity (m s^{-1}). We applied a Nikuradse roughness (k_s) of 0.01 m previously applied by Le Hir et al. (2000) on the Brouage mudflat. The bottom roughness z_0 was equal to $\frac{k_s}{30}$. The wave BSS (τ_w, Pa) was calculated according to the formula of Soulsby (1997):

$$\tau_w = 0.5 \rho f_w U_b^2, \tag{7}$$

where U_b is the wave orbital velocity (m s^{-1}) and f_w is the wave friction coefficient. f_w was calculated according to the formula of Swart (1974):

$$f_w = 0.3, \text{if} r \leq 1.57, \tag{8}$$

$$f_w = 0.00251 \; exp\left(5.21 r^{-0.19}\right), \text{if } r > 1.57, \tag{9}$$

where r is the relative roughness related to the wave excursion A (m) and the Nikuradse roughness:

$$r = \frac{A}{k_s}, \text{with } A = \frac{U_b T}{2\pi}, \tag{10}$$

where T is the wave period (s). The average BSS (τ_m) and the maximum BSS (τ_{max}) were calculated according to the formulation of Soulsby (1997), which takes into account nonlinear interactions between waves and currents:

$$\tau_m = \tau_c \left[1 + 1.2\left(\frac{\tau_w}{\tau_c + \tau_w}\right)^{3.2}\right], \text{and} \tag{11}$$

$$\tau_{\max} = \left[\left(\tau_m + \tau_w \cos\phi \right)^2 + \left(\tau_w \sin\phi \right)^2 \right]^{\frac{1}{2}}, \tag{12}$$

where ϕ is the angle (°) between waves and currents direction.

2.3.5. The MPB Resuspension

The model previously used in Savelli et al. (2018) was modified to take into account the explicit representation of the hydrodynamically and wave-driven MPB resuspension mechanisms. We set the loss rate of MPB biomass in the sediment to 0.001 hr^{-1} during high tides. The constant represents MPB senescence and the grazing by subsurface deposit feeders. We related the resuspension of MPB biomass to the simulated $\tau_{\max}$, which combined τ_w and τ_c. During high tides, three different resuspension scenarios were modulated by BSS thresholds. First, the critical BSS for fluff layer resuspension ($\tau_{\text{crit}_{\text{fluff}}}$) was set at 0.015 Pa (Orvain et al., 2004). Second, the critical BSS for massive resuspension ($\tau_{\text{crit}_{\text{mass}}}$) was set according to the critical BSS for bare sediment (τ_{baresed}), consolidated by the total MPB biomass (mg Chl *a* m^{-2}; Mariotti & Fagherazzi, 2012):

$$\tau_{\text{crit}_{\text{mass}}} = \tau_{\text{baresed}} + \left[\omega \times (F + S) \right], \tag{13}$$

where ω is the consolidation coefficient of the bare sediment by the MPB biomass [Pa(mg Chl *a* $m^{-2})^{-1}$].

During immersion periods,

- if $\tau_{\max} < \tau_{\text{crit}_{\text{fluff}}}$, no resuspension occurred. Immersed MPB cells achieved the downward migration from *S* to *F* and *P. ulvae* individuals were still active (grazing and bioturbating);
- if $\tau_{\text{crit}_{\text{fluff}}} < \tau_{\max} < \tau_{\text{crit}_{\text{mass}}}$, *P. ulvae* individuals were not grazing and bioturbating any more and only the fluff layer was eroded at the rate:

$$\frac{dB}{dt} = -\phi B \times \left[\frac{\tau_{\max}}{\tau_{\text{crit}_{\text{mass}}}} - 1 \right], \tag{14}$$

  where ϕ is the erosion coefficient of the fluff layer (s^{-1}) and $\left[\frac{\tau_{\max}}{\tau_{\text{crit}_{\text{mass}}}} - 1 \right]$ represents the intensity of the resuspension.
- if $\tau_{\max} > \tau_{\text{crit}_{\text{mass}}}$, the resuspension was considered massive and all the MPB compartments (sediment, biofilm, and fluff layer) were impacted by resuspension. *P. ulvae* individuals were inactive. Both the surface biofilm and the fluff layer were fully resuspended. The Partheniades-Ariathurai law (Ariathurai & Krone, 1976; Partheniades, 1962) for mud erosion was used to determined the MPB biomass resuspension from the sediment:

$$E = E_0 \times \left[\frac{\tau_{\max}}{\tau_{\text{crit}_{\text{mass}}}} - 1 \right]^n, \tag{15}$$

where E and E_0 are the sediment erosion rate ($kg{\cdot}m^{-2}{\cdot}s^{-1}$) and the erosion constant ($kg{\cdot}m^{-2}{\cdot}s^{-1}$), respectively. n is a power function of the sediment composition (for mud, $n = 1$). The MPB biomass in the sediment (mg Chl *a* m^{-2}) was converted into Chl *a* concentration per mass of sediment (F^*, mg Chl *a* kg^{-1} dry sediment) using a constant bulk density of sediment (520 g L^{-1}). The resulting MPB erosion rate (E_{MPB}, mg Chl $a{\cdot}m^{-2}{\cdot}s^{-1}$) is as follows:

$$E_{\text{MPB}} = E_0 \times F^* \times \left[\frac{\tau_{\max}}{\tau_{\text{crit}_{\text{mass}}}} - 1 \right]^n, \tag{16}$$

The occurrence of the massive resuspension events also depended on the MPB biomass remaining in the sediment first centimeter. In case of a massive resuspension event, a background of MPB biomass (F_{mini}, mg Chl *a* m^{-2}) was always kept in the sediment to allow the biomass recovery after the event. If $F > F_{\text{mini}}$, E_{MPB} and all the surface biofilm and fluff layer were eroded. Otherwise, only the fluff layer was integrally resuspended.

The physical and biological constants used in this study are given in Table 2. The differential equations of the biological model without wave- and tidal-induced MPB resuspension are fully detailed in Savelli et al. (2018). The physical-biological coupled model was run at the study site from 1 September to 31 December 2011 for the spin-up and from 1 January to 31 December 2012 for the analysis. *F* and *Z* were initially set to 100 mg Chl *a* m^{-2} and 500 mg C m^{-2}, respectively. The differential equations were solved with the fourth-order Runge-Kutta method with a 6-min time step. The model run with the explicit representation of wave- and tidal-induced MPB resuspension (PHY_{run}) was compared to a reference run (REF_{run}) with a constant rate

Table 2
Physical and Biological Model Parameters Related to the MPB Resuspension

Symbol	Description	Value	Unit	Source
Physics				
$\tau_{baresed}$	Critical BSS for bare sediment	0.3	Pa	Present study
$\tau_{crit_{fluff}}$	Critical BSS for fluff layer erosion	0.015	Pa	Orvain et al. (2004)
k_s	Nikuradse roughness	0.01	m	Le Hir et al. (2000)
E_0	Mud erosion constant	2×10^{-5}	$kg{\cdot}m^{-2}{\cdot}s^{-1}$	Present study
ω	Consolidation factor by MPB biomass	0.006	$Pa(mg\ Chl\ a\ m^{-2})^{-1}$	Present study
Biology				
γ	Mean time spent by a MPB cell at the surface	1	hr	Blanchard et al. (2004)
F_{mini}	Background MPB biomass	73	mg Chl a m^{-2}	Present study
υ	*P. ulvae* crawling rate	1.2×10^{-9}	$m^2{\cdot}s^{-1}{\cdot}ind^{-1}$	Present study
B_{max}	Saturation of Chl a concentration in the fluff layer	11.5	mg Chl a m^{-2}	Orvain et al. (2007)

of MPB resuspension during high tides without any parametrization of biologically consolidated sediment was used. The setup of the REF_{run} is detailed in Savelli et al. (2018).

Finally, we tested the sensitivity of the simulated MPB PP and instantaneous resuspension to simultaneous variations of key biological and physical constants. Random values of the bed roughness length (z_0), critical BSS for resuspension of bare sediment ($\tau_{baresed}$), consolidation factor (ω), erosion constant of pure mud (E_0), minimum MPB biomass in the sediment (F_{mini}), and mean time spent by a MPB cell at the sediment surface (γ) were selected within the observed ranges (Table 3) by a Monte Carlo fixed sampling method (Hammersley & Handscomb, 1964). The method aims to quantify how simultaneous variations of key biological constants might impact the simulated MPB production and instantaneous resuspension (see Savelli et al., 2018). A total of 10,000 model runs was performed using the same set of initial conditions.

Table 3
Range of Values for the Random Selection of the Model Constants Used in the Monte Carlo Sensitivity Analysis

Parameters	Units	Range	Source
z_0	m	$[2 \times 10^{-4}; 1.65 \times 10^{-2}]$	Ke et al. (1994) Le Hir et al. (2000) Verney et al. (2006)
E_0	$kg\ m^{-2}\ s^{-1}$	$[1 \times 10^{-5}; 1 \times 10^{-3}]$	Mengual et al. (2017) and references within
$\tau_{baresed}$	Pa	[0.05; 1]	Mariotti and Fagherazzi (2012) and references within
ω	$Pa(mg\ Chl\ a\ m^{-2})^{-1}$	[0.001; 0.02]	Mariotti and Fagherazzi (2012) and references within
F_{mini}	mg Chl a m^{-2}	[35; 100]	Guarini et al. (2000) Blanchard et al. (2002) Herlory et al. (2004) Blanchard et al. (2006) Orvain et al. (2014)
γ	h	[0.25; 1.5]	Blanchard et al. (2004)

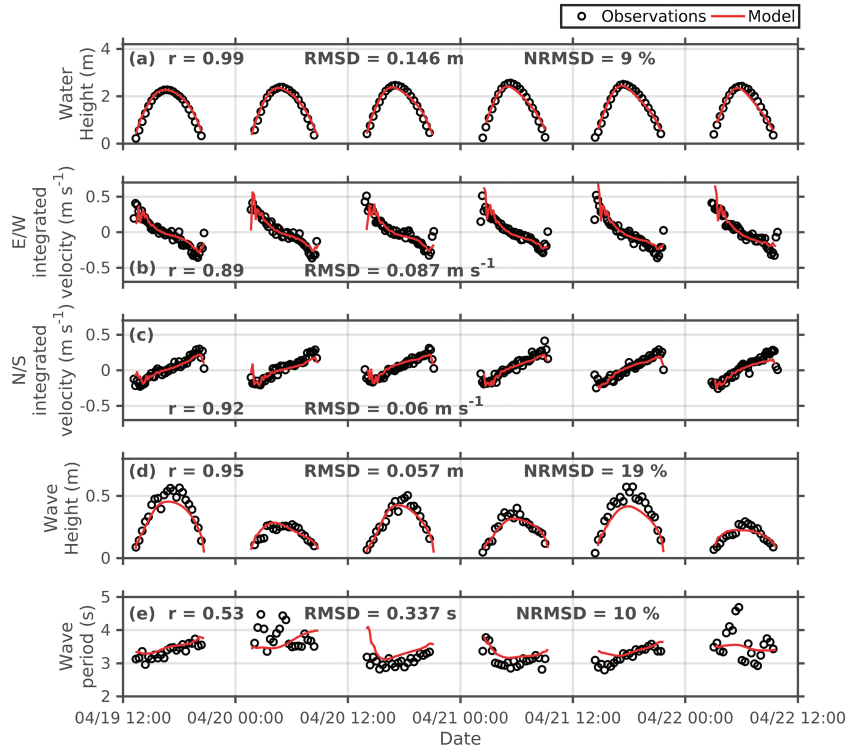

Figure 3. Measured and simulated (a) water height, (b) east-west velocity current component, (c) north-south current velocity component, (d) significant wave height, and (e) wave period of the second moment at the study site between 19 and 22 April 2012. *r* is the Pearson's correlation coefficient. RMSD and NRMSD are the root-mean-square error and the normalized root-mean-square error.

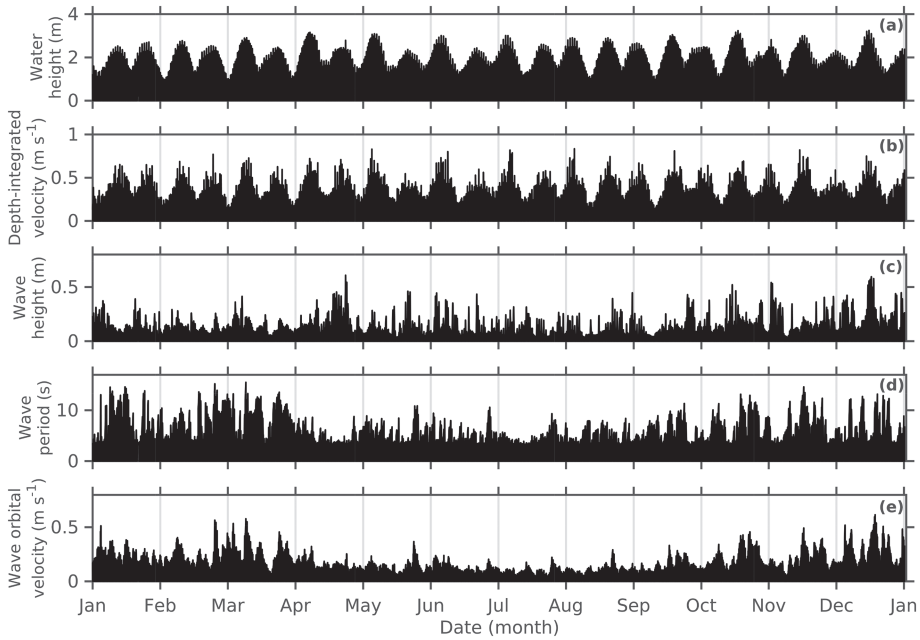

Figure 4. Time series of the 2012 simulated (a) water height, (b) depth-integrated velocity, (c) significant wave height, (d) wave period of the second moment, and (e) wave orbital velocity.

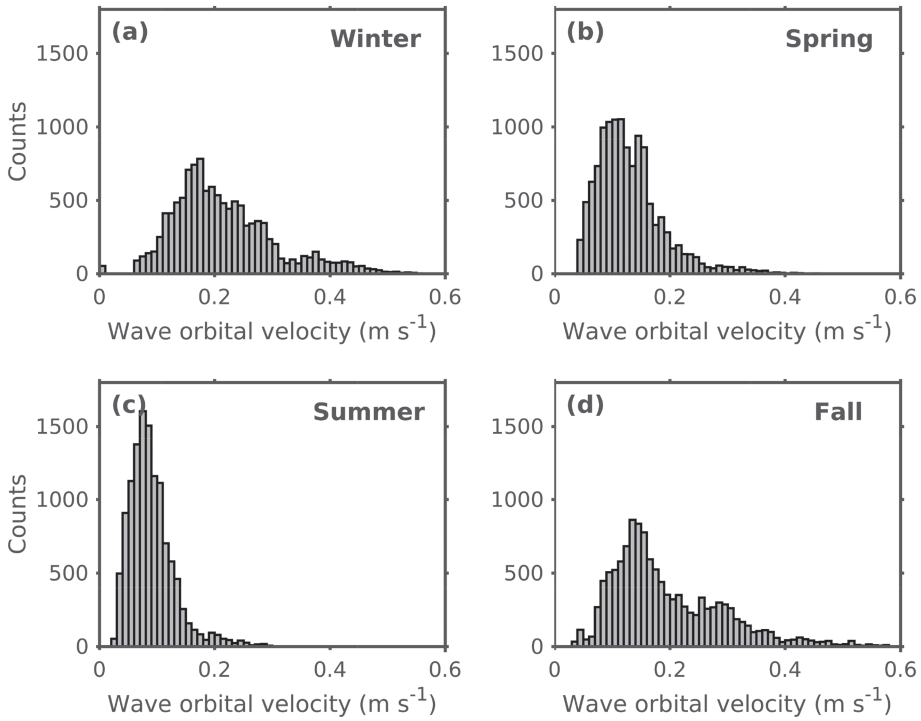

Figure 5. Histograms of the 2012 simulated wave orbital velocity in (a) winter, (b) spring, (c) summer, and (d) fall.

3. Results

3.1. Physical Conditions

In situ water height and current velocity derived from ADCP measurements in April 2012 were used to compute the 10-min mean significant wave height and mean wave period that were compared to the model data (Figure 3). The model simulated well the high-frequency (10 min) variations of the water height (RMSD = 0.14 m, NRMSD = 9%) and current velocity components. The RMSD was 0.087 m s^{-1} for the east-west component and 0.06 m s^{-1} for the north-south component (Figure 3). With respect to the wave height and mean wave period, the RMSD was 0.057 m and 0.337 s, respectively (Figure 3). It corresponded to NRMSD of 19% and 10%, respectively.

The water height and depth-integrated velocity simulated by the model in 2012 varied fortnightly with the tidal cycle (Figure 4). During neap tides, the simulated water height and current velocity reached 1.42 m and 0.41 m s^{-1}, respectively. During spring tides, they were higher and reached 3.24 m and 0.83 m s^{-1}, respectively.

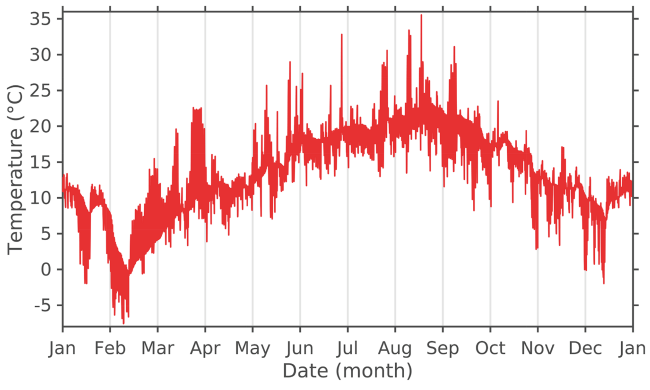

Figure 6. Simulated mud surface temperature (°C) in 2012.

The simulated wave period ranged from 3 to 15.5 s (Figure 4). The simulated wave height and orbital velocity varied by several orders of magnitude, ranging between 2×10^{-3} m and 0.61 m and between 5×10^{-3} m s^{-1} and 0.62 m s^{-1}, respectively (Figure 4). The median wave orbital velocity was 0.14 m s^{-1}. High values of wave orbital velocity (i.e., higher than the median) were more frequently reached during winter and fall compared to spring and summer (Figure 5).

During winter, the simulated MST was 6.2 ± 4.3 °C in average (Figure 6). The simulated mean MST was more than twice in summer reaching 20.4 ± 2.8 °C (Figure 6). It was comparable in spring and fall with 14.2 ± 3.5 °C and 12.4 ± 3.8 °C, respectively (Figure 6).

3.2. MPB and *P. Ulvae* Dynamics

The total simulated MPB biomass (MPB biomass in the biofilm and the MPB biomass in the sediment) reached a seasonal maximum on 1 May

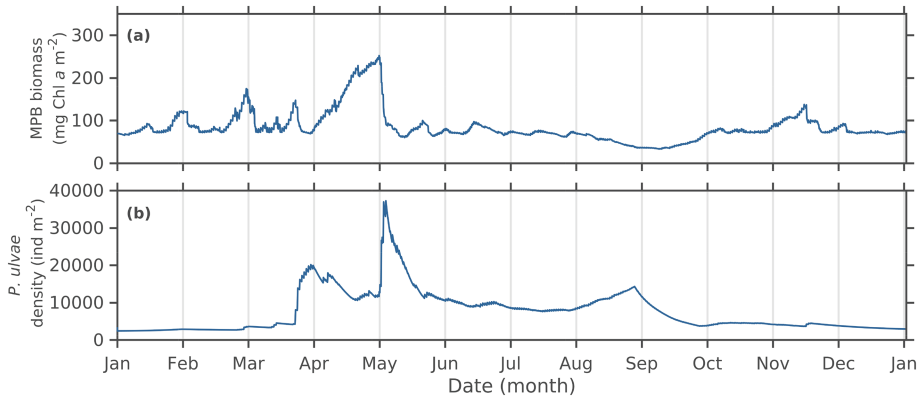

Figure 7. Time series of the 2012 simulated (a) total MPB biomass (mg Chl *a* m^{-2}) and (b) *P. ulvae* density (ind m^{-2}).

(252 mg Chl *a* m^{-2}; Figure 7a). This peak is preceded by three peaks of simulated MPB biomass around 150 mg Chl *a* m^{-2} on 30 January, 29 February, and 23 March (Figure 7a). In summer, the simulated MPB biomass decreased below 100 mg Chl *a* m^{-2}. In fall, one peak of MPB biomass of moderate intensity (137 mg Chl *a* m^{-2}) occurred on 14 November (Figure 7a). The peaks of MPB biomass simulated in March and April were tightly followed by two seasonal peaks of simulated *P. ulvae* density (~20,100 and 37,000 ind m^{-2}, respectively; Figure 7b) during which the simulated MST (19.5 °C and 17.6 °C) was close to the optimal temperature for *P. ulvae* grazing (20 °C). In fall, the simulated *P. ulvae* density was low (~3,500 ind m^{-2}; Figure 7b).

3.3. MPB Biomass Resuspension

3.3.1. Model Validation

The modeled resuspended MPB Chl *a* was normalized by the water height and compared to the time-coincident in-water Chl *a* concentration provided by remote sensing and in situ water samples from two monitoring stations (Figures 1 and 8). Both in situ and satellite observations favorably compared with the simulated resuspended Chl *a*. Whatever the source of data (model output, in situ sampling, or remote sensing), the in-water Chl *a* concentration exhibited a consistent seasonal variability with higher value in winter-spring than in summer-fall. The simulated maximum peaks of resuspended MPB (from 5–45 mg Chl *a* m^{-3}) generally compared to satellite estimates (1.4–35.4 mg Chl *a* m^{-3}). In particular, the height of peaks occurring from late February to early March was consistent with satellite observations (30 ± 18 mg Chl *a* m^{-3}, 28 February; Figure 8). In fall and winter, the lower concentration of resuspended MPB (2.44 ± 7 mg Chl *a* m^{-3}) was in agreement with in situ measurements (2.1 ± 1 mg Chl *a* m^{-3}; Figure 8). All together, the reasonable agreement between simulation outputs, satellite estimates, and in situ observations is very encouraging. In order to better understand the temporal dynamics of MPB resuspension, we now analyze in more details the time series of MPB resuspension using high-frequency simulations.

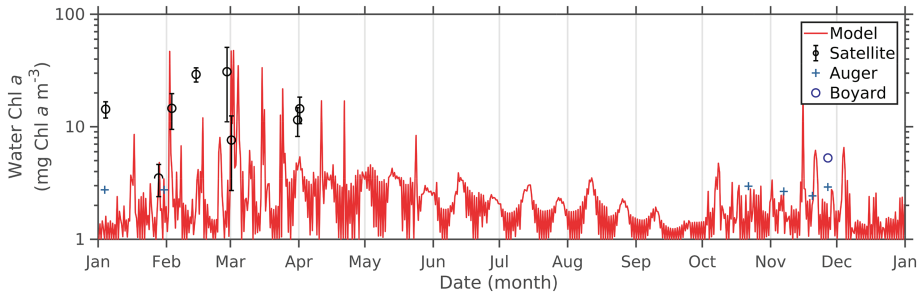

Figure 8. Time series of the 2012 simulated and observed remotely sensed and measured in situ in-water Chl *a* concentration (mg Chl *a* m^{-3}). The simulated resuspended MPB biomass was cumulated over each high tide and normalized over the corresponding maximal water depth.

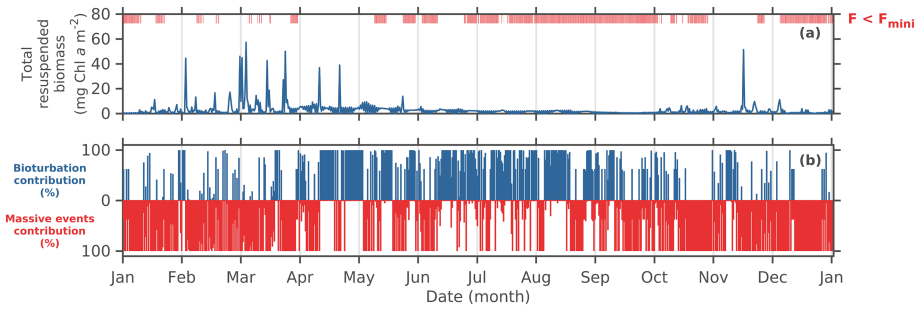

Figure 9. Time series of the 2012 simulated (a) total resuspended MPB biomass (mg Chl *a* m^{-2}) and (b) relative contribution (%) of resuspended MPB biomass through bioturbation (blue) and massive events (red). The simulated resuspended MPB biomass was cumulated over each high tide.

3.3.2. Temporal Variability

MPB resuspension was highly variable in terms of seasonal occurrence and quantity and did not systematically occur during each tidal cycle (Figure 9). The instantaneous resuspended biomass was in average 0.04 ± 0.45 mg Chl *a* m^{-2}. The instantaneously resuspended MPB water column-normalized concentration peaked to 110 mg Chl *a* m^{-3} on 1 February. Over a high tide, the rate of MPB erosion averaged 0.4 ± 0.85 mg Chl *a* m^{-2} hr^{-1} with a maximum of 8.93 mg Chl *a* m^{-2} hr^{-1} on 12 November.

3.3.3. Massive Resuspension

Interestingly, the seasonal variation of the MPB resuspension was mainly driven by massive resuspension events. Massive resuspension represented 70% of the MPB biomass resuspended annually, which was exported to the water column in 37 days only (Tables 4 and 5). Massive resuspension mostly occurred during winter and fall, as evidenced by a mean contribution of 80% to total resuspended MPB biomass (Figure 9b). The contribution of such events relative to total resuspension was the highest during winter (613 mg Chl *a* m^{-2}, Table 4). In winter, 18 days (457 events) of massive resuspension were responsible of the export to the water column of 32% of the total annually resuspended MPB biomass (Table 4). The same trend was also observed during spring, when 5.8 days (363 events) of massive resuspension contributed to 20% of the total annually resuspended MPB biomass (Table 4). On the contrary, massive resuspension was rare during summer (only 192 events) and did not substantially contribute to the total annual export of MPB to the water column (Table 4). In the model, spring tides were isolated by considering tides with a maximal water depth >1.8 m. Beside the above-mentioned seasonal pattern, it is noteworthy to report that 60% of the annual MPB export from the sediment to the water column occurred during spring tides.

3.3.4. Chronic Resuspension

In contrast, the MPB biomass resuspended in the model through bioturbation contributed to only 30% of the total annual water column export (Table 4). Resuspension through bioturbation mainly occurred from late March to September (Figure 9b and Table 4), when *P. ulvae* individuals were active and abundant in the model (Figure 7b). Fluff layer mediated export of MPB corresponded to 46 days of resuspension and 392 events (Table 4). In spring, fluff layer MPB resuspension (337 mg Chl *a* m^{-2}) compared to that of massive resuspension (381 mg Chl a m^{-2}) but was threefold more frequent. In summer, the fluff layer resuspension (157 mg Chl *a* m^{-2}) was higher than massive resuspension (78 mg Chl *a* m^{-2}), which was only episodic (<2

Table 4
Simulated MPB Biomass Resuspended ($\sum_{RES}$) in 2012 Through Bioturbation and Massive Events, and Frequency ($Freq_{RES}$), Duration (Dur_{RES}), and Number (N) of the Simulated Events

	Massive resuspension				Fluff layer resuspension			
Season	$\sum_{RES}$ (mg Chl *a* m^{-2})	$Freq_{RES}$ (%)	Dur_{RES} (day)	*N*	$\sum_{RES}$ (mg Chl *a* m^{-2})	$Freq_{RES}$ (%)	Dur_{RES} (day)	*N*
Winter	613.1	20	18	457	34.4	5	4.6	73
Spring	381.3	6.3	5.8	363	337.7	22.6	20.8	120
Summer	78.4	1.7	1.54	192	157.6	19	17.3	129
Fall	283.7	12.7	11.6	492	41.7	4	3.5	70
Annual	1,355.5	10	37	1,504	571.3	12.6	46.2	392

Table 5
Simulated Total Resuspended MPB Biomass ($\sum_{RES}$), Frequency ($Freq_{RES}$) and Duration (Dur_{RES}) of the Resuspension Events, and MPB PP in the REF_{run} and the PHY_{run} in 2012

Season	$\sum_{RES}$ (g C m^{-2})	$Freq_{RES}$ (%)	Dur_{RES} (day)	PP (g C m^{-2})	$\sum_{RES}$:PP (%)
REF_{run}					
Winter	10.3	53	48.6	34	30.3
Spring	8.1	56	51.4	47.2	17.2
Summer	5.6	55	50.6	41	13.7
Fall	6.2	56	51	29.3	21.7
Annual	30.2	55	201.6	151.5	19.9
PHY_{run}					
Winter	15.9	25	22.6	28.4	56
Spring	27.9	29	26.6	67.6	41.3
Summer	9.61	20	18.8	26	37
Fall	7.38	16.6	15.1	18.6	39.7
Annual	60.8	22	83.2	140.5	43.3

days). Annually, the number of fluff layer resuspension events (392 events) were lower than the massive resuspension events (1,504 events; Table 4). However, the fluff layer resuspension events were longer (46.2 days) than the synoptic and shorter massive resuspension events (37 days; Table 4).

3.3.5. Resuspended MPB Biomass and MPB PP

In order to assess the impact of wave- and tidal-induced resuspension on MPB dynamics, we compared the time-integrated total resuspended MPB biomass and MPB PP simulated in 2012 (PHY_{run}) with the reference run where the rate of MPB resuspension is constant during high tides (REF_{run}). The total resuspended MPB biomass was twice in the PHY_{run} (60.8 g C m^{-2}) than in the REF_{run} (30.2 g C m^{-2}; Table 5). The seasonal variability also differs between the two series of simulations. In the PHY_{run}, the resuspended MPB biomass was the highest in spring (27.9 g C m^{-2}) and the lowest in fall (7.38 g C m^{-2}; Table 5). On the contrary, in the REF_{run}, the resuspended MPB biomass was the highest in winter (10.3 g C m^{-2}) and the lowest in summer (5.6 g C m^{-2}; Table 5), and the amplitude of the seasonal difference was twice lower than in the PHY_{run}. In the REF_{run}, the frequency (53–56%) and duration (48.6–51.4 days) of MPB resuspension events were similar throughout all the seasons (Table 5). By contrast, in the PHY_{run}, summer and fall were characterized by the lowest seasonal MPB resuspension frequency (20% and 16.6%, respectively) and duration (18.8 days and 15.1

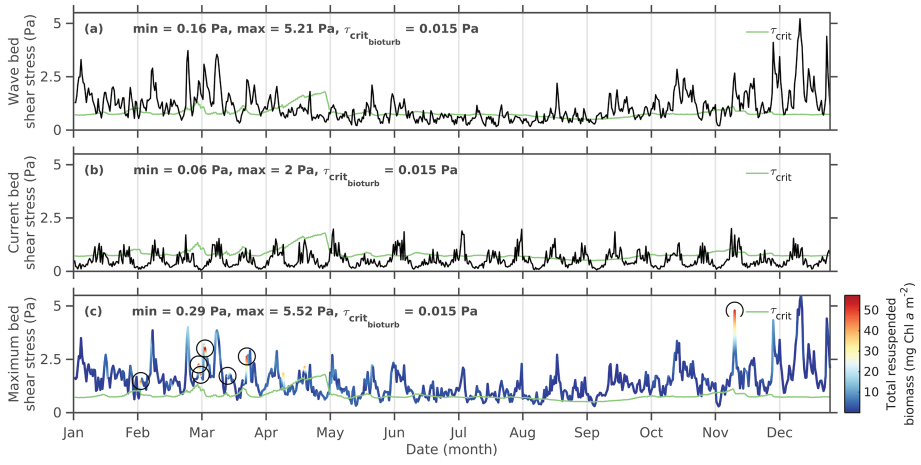

Figure 10. Time series of the 2012 simulated (a) wave BSS, (b) current BSS, and (c) maximum BSS along with the total resuspended MPB biomass. The green line represents the critical BSS for massive resuspension events. Dark circles indicate resuspended biomass higher than the last percentile of the resuspended MPB biomass simulated time series in 2012 (40.6 mg Chl *a* m^{-2}). Note that only maximum values of BSS per tidal cycle are shown.

Table 6
Simulated Frequency of Waves, Tidal Current, and Combined Waves and Current Maximal BSS Higher than the Critical BSS in 2012

Season	Waves (%)	Current (%)	Combined waves and current (%)
Winter	36	0.22	36.2
Spring	13	0.18	13.4
Summer	10	0.5	11.5
Fall	34	0.28	34.6
Annual	23	0.30	23.7

days, respectively; Table 5), whereas the frequency and duration of resuspension events were both higher during spring (respectively 29% and 26.6 days).

With respect to MPB PP, the annual rate was close both in the PHY_{run} (140.5 g C m^{-2}) and the REF_{run} (151.5 g C m^{-2}; Table 5). In both runs, PP was the highest in spring (47.2 g C m^{-2} in the REF_{run} and 67.6 g C m^{-2} in the PHY_{run}). PP simulated in spring departed more from the other seasons in the PHY_{run} than in the REF_{run}. In the PHY_{run}, the spring PP was 2.3-fold to 3.6-fold higher than in other seasons (Table 5). At the annual scale, 43.3% (PHY_{run}) and 19.9% (REF_{run}) of the PP was resuspended (Table 5). At the seasonal scale, PP was resuspended the most in winter and the least in summer in both runs (Table 5). In winter, PP was relatively low, while the resuspended biomass was high. In the PHY_{run}, high resuspended MPB biomass resulted from more frequent intense hydrodynamical disturbances combined with moderate MPB biomass in winter (Figure 9a). Such a pattern led to a moderate consolidation of the sediment (0.82 ± 0.13 Pa; Figure 10). In contrast, in summer, PP was slightly lower than in winter but the level of resuspended biomass was much lower due to less frequent intense hydrodynamic disturbances and lower MPB biomass in the sediment than in winter. This pattern was simulated although the sediment was relatively unconsolidated (0.64 ± 0.08 Pa; Figure 10).

3.4. Drivers of MPB Resuspension

3.4.1. Waves and Currents BSS

The critical BSS for massive resuspension ($\tau_{crit_{mass}}$) was compared to the wave BSS (τ_w) and, current BSS (τ_c) and to the maximal BSS (τ_{max}), which combined both current and wave BSS. As MPB had a consolidating effect on the sediment, $\tau_{crit_{mass}}$ was set to covary with MPB biomass in the model. As a result, $\tau_{crit_{mass}}$ displayed a seasonal variation similar to that of MPB biomass (Figure 7 and 10): winter-spring maximum (with four peaks from 1 to 1.8 Pa) and summer minimum (0.64 ± 0.08 Pa). Overall, τ_{max} exceeded $\tau_{crit_{mass}}$ at a similar frequency than τ_w.

In contrast to the massive resuspension BSS, τ_w was more variable and exhibited more peaks in winter (1.15 ± 0.6 Pa) and fall (1.1 ± 0.75 Pa) than in spring (0.65 ± 0.34 Pa) and summer (0.43 ± 0.25 Pa; Figure 10a).

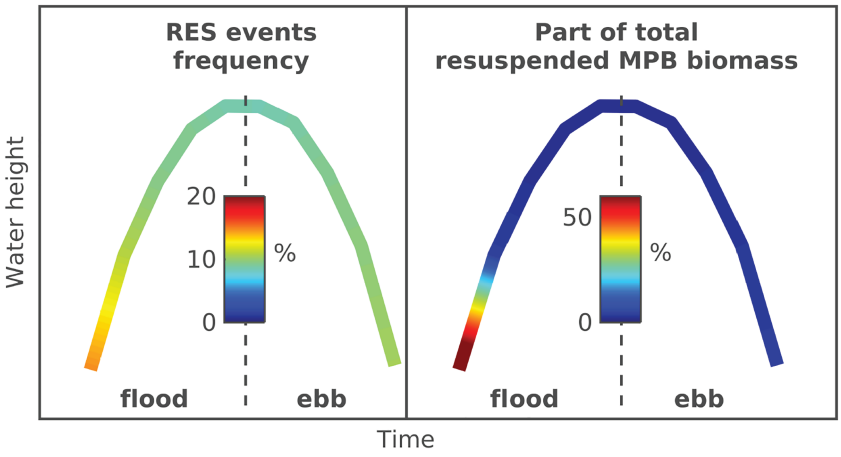

Figure 11. Frequency of the resuspension events simulated in 2012 and the relative distribution of the total resuspended MPB biomass over a high tide.

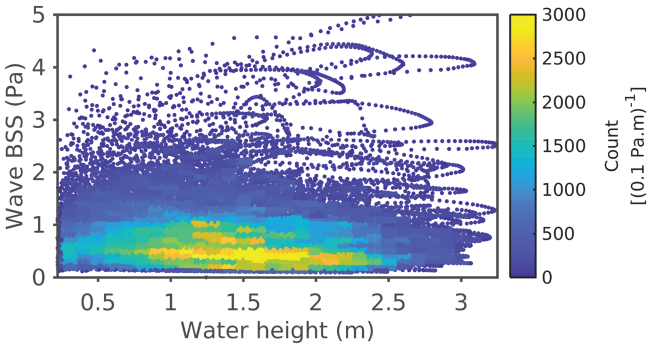

Figure 12. Relationship between the simulated wave BSS and the water depth.

During the studied year, τ_w exceeded $\tau_{crit_{mass}}$ during 84 days. The dominance of τ_w was higher in winter (36%) and fall (34%) than during summer (10%; Table 4). The current BSS was generally lower (annual average of 0.1 ± 0.13 Pa) than τ_w (annual average of 0.8 ± 0.6 Pa) and displayed values similar to that of $\tau_{crit_{mass}}$ during each season (Table 6). As τ_c was driven by tidal dynamics, it reached a maximum and was as high as $\tau_{crit_{mass}}$ during spring tides (Figure 10b).

3.4.2. Resuspension Intensity

In order to relate MPB dynamics with BSS, the highest MPB resuspension events (corresponding to the last percentile of the resuspended MPB biomass simulated time series, that is, higher than 40.6 mg Chl *a* m^{-2}) were highlighted in Figure 10c by dark circles. All the seven highest resuspension events occurred during November or February–March. Three of them were responsible for the export to the water column of ~150 mg Chl *a* m^{-2} in early March (Figure 10c). They were followed by a drop in $\tau_{crit_{mass}}$, which was due to a decrease in MPB biomass within the sediment. Though the decrease in MPB biomass contributes to lessen the sediment consolidation (Figure 7), strong resuspension events did not occur during summer (Figure 10c). The lowest maximal value reached by τ_{max} during high tides of 2012 was 0.29 Pa (Figure 10b). $\tau_{crit_{fluff}}$ (0.015 Pa) was therefore exceeded at each high tide. The simulated fluff layer was therefore always eroded at least one time during immersion periods.

Over a tidal cycle, most of the simulated resuspension events occurred at the flood beginning (14%) and at the end of ebb (10%; Figure 11). These moments correspond to low water height when τ_w was maximized until around 1–1.25 m of seawater depth (Figure 12). Most of the simulated total resuspended MPB biomass (76%) was exported at the flood beginning (Figure 11).

3.4.3. MPB PP and Resuspension, *P. ulvae* Ingestion

In order to relate the resuspended MPB biomass with the MPB growth conditions, the simulated daily MPB resuspension was compared to the simulated daily MPB PP and to the simulated daily *P. ulvae* ingestion (Figure 13b). PP increased during winter-spring and reached a maximum in late March (~1.6 g C m^{-2} day^{-1}; Figure 13). It resulted into an increase of MPB biomass in the sediment (Figure 13a). The simulated decreases of the MPB biomass in early March, late March, and early May were driven by strong resuspension and/or by *P. ulvae* ingestion events (Figure 13). Seven peaks of daily resuspension (1–2.2 g C m^{-2} day^{-1}) occurred in winter, spring and fall (Figure 13b). By comparison, the daily *P. ulvae* ingestion exhibited two peaks, one of them reaching a maximum of 4.1 g C m^{-2} day^{-1} in early May (Figure 13b). The yearly integrated resuspension of MPB (60.8 g C·m^{-2}·yr^{-1}) was 1.3-fold higher than the yearly integrated *P. ulvae* ingestion (41.1 g C·m^{-2}·yr^{-1}). The loss of MPB biomass by resuspension was therefore higher than the loss by grazing by *P. ulvae*.

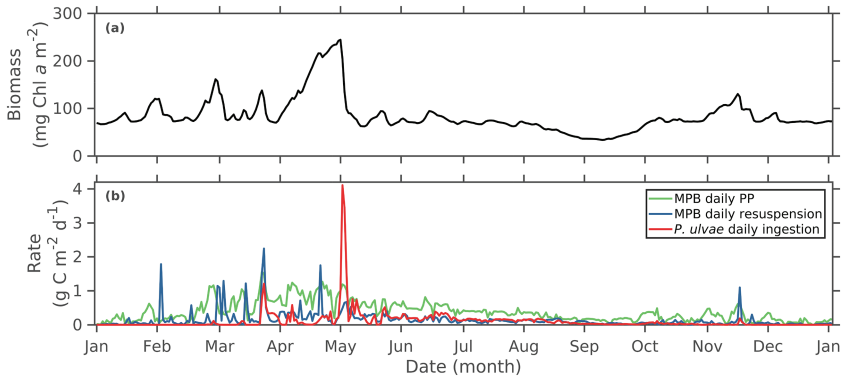

Figure 13. Time series of the 2012 simulated (a) MPB biomass in the first centimeter of sediment (mg Chl *a* m^{-2}) and (b) daily PP rate (g C m^{-2} day^{-1}), daily resuspension of MPB biomass (g C m^{-2} day^{-1}), and daily ingestion of *P. ulvae* (g C m^{-2} day^{-1}).

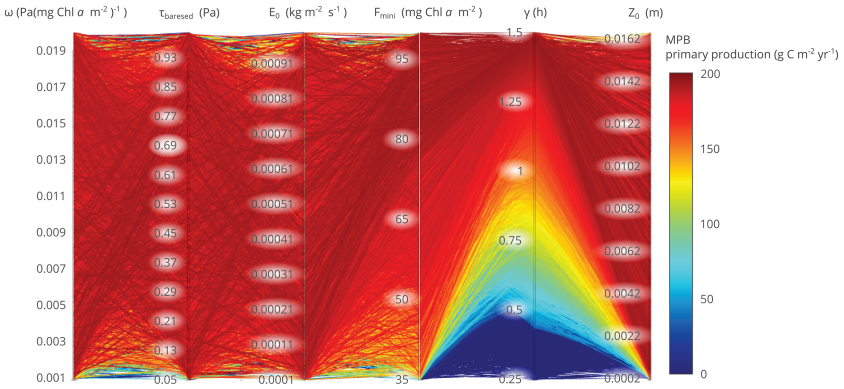

Figure 14. Parallel coordinates of the simulated MPB primary production (g C·m^{-2}·yr^{-1}) according to the consolidation factor of sediment by the MPB biomass (ω), the critical BSS for the resuspension of bare sediment (τ_{baresed}), the erosion constant (E_0), the background MPB biomass (mg Chl a m^{-2}), the average time spent by MPB cells at the surface (γ), and the bed roughness (z_0) for 10,000 combinations run in the Monte Carlo sensitivity analysis.

3.5. Sensitivity Analysis

A total of 10,000 simulations was run using random sets of biological (F_{mini}, γ) and physical (ω, τ_{baresed}, E_0, z_0) constants varying within the reported observed ranges (Table 3). This approach was used in Savelli et al. (2018). The constants were chosen as they shape the simulated MPB production and the occurrence and rate of MPB resuspension. Figures 14 and 15 show the 10,000 parameters combinations and the resulting simulated MPB annual PP and maximal instantaneous resuspension.

Except for γ, a high annual MPB PP was simulated in all regions of the tested ranges of F_{mini}, ω, τ_{baresed}, E_0 and z_0 (Figure 14). The annual PP was the most sensitive to γ (Figure 14). This constant set the duration of the time spent by the MPB biofilm at the sediment surface for the next low tide. The higher was γ, the higher was the annual PP. Below 25 min spent at the sediment surface, the annual PP reached critical values (PP < 50 g C·m^{-2}·yr^{-1}; Figure 14).

The instantaneous rate of MPB biomass resuspension was also sensitive to γ when it took values lower than 25 min (Figure 15). A low PP resulting from a low γ value led to the decline of the MPB biomass in the sediment and resuspended MPB biomass. When γ was higher than 25 min, the MPB resuspension was sensitive to ω, E_0 and τ_{baresed} (Figure 15).

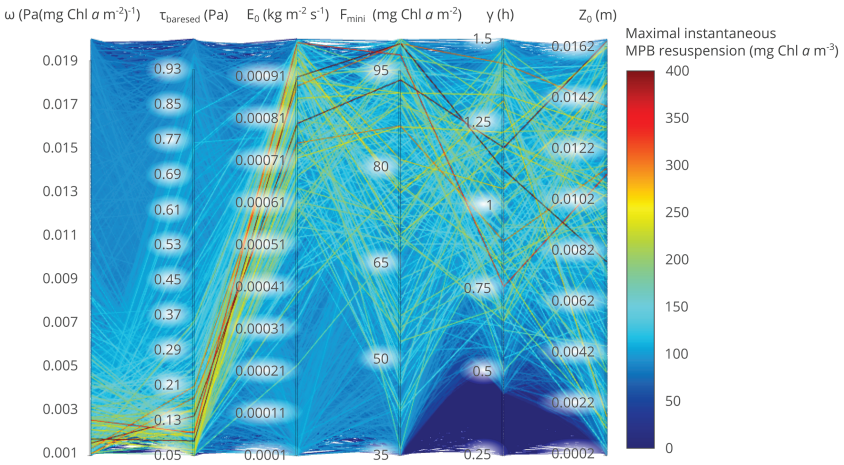

Figure 15. Parallel coordinates of the simulated instantaneous resuspension of MPB biomass (mg Chl a m^{-3}) according to the consolidation factor of sediment by the MPB biomass (ω), the critical BSS for the resuspension of bare sediment (τ_{baresed}), the erosion constant (E_0), the background MPB biomass (mg Chl a m^{-2}), the average time spent by MPB cells at the surface (γ), and the bed roughness (z_0) for 10,000 combinations run in the Monte Carlo sensitivity analysis.

An increase of ω and E_0 combined with a decrease of $\tau_{baresed}$ resulted into a higher maximal instantaneous resuspension of MPB (Figure 15). The strongest resuspension events (>200 mg Chl *a* m^{-3}) occurred for ω, E_0 and $\tau_{baresed}$ values ranging between 0.001 and 0.005 Pa (mg Chl *a* m^{-2}), 5.5 $\times 10^{-4}$ to 1 $\times$ 10^{-3} kg m^{-2} s^{-1} and 0.4 and 1 Pa, respectively (Figure 15).

Overall, the simulated annual MPB PP was mainly sensitive to γ. When PP was relatively high (γ > 25 min), the MPB resuspension was mostly sensitive to the sediment erodibility constants ω, E_0, and $\tau_{baresed}$, as they constrained the occurrence and rate of MPB resuspension.

4. Discussion

4.1. The Seasonal Cycle of MPB Resuspension

The dynamics of the simulated MPB resuspension relies on the seasonal cycle of MPB biomass in the sediment. Here, we used the model of Savelli et al. (2018), which reasonably simulates the MPB dynamics in the sediment for the year 2008. The simulated seasonal cycle of MPB biomass is characterized by a spring bloom, a summer depression and a moderate fall bloom. According to Savelli et al. (2018), the spring bloom of MPB biomass was driven by a high PP triggered by MST close to the MPB temperature optimum for photosynthesis and an increasing solar irradiance from late winter to the end of spring. In summer, the combined effect of a low thermoinhibited MPB PP and a moderate but sustained grazing pressure was responsible for a low MPB PP and biomass (Savelli et al., 2018). In fall, the absence of grazing and a lower simulated MST than in summer led to a moderate bloom of biomass that declined rapidly due to decreasing light levels (Savelli et al., 2018). The total MPB biomass simulated within the first centimeter of sediment exhibited a seasonal pattern consistent with that previously observed in other northern European mudflats (i.e., van der Wal et al., 2010; Echappé et al., 2018). The simulated synoptic events of MPB resuspension superimposed on the MPB intrinsec seasonal cycle of MPB biomass and PP.

The model suggests a high seasonal MPB resuspension during winter and spring. In their study on the South Korean Nanaura mudflat, Koh et al. (2007) sampled the MPB Chl *a* concentration in the sediment and the suspended particulate matter to derive resuspended benthic Chl *a* concentration in seawater from July 2002 to February 2003. The measured Chl *a* concentration in the sediment and the resuspended benthic Chl *a* were higher during winter than in summer and fall in line with our results. On the same study site, Koh et al. (2006) estimated the highest concentrations of resuspended Chl *a* during spring tides, which is consistent with the high MPB export from the sediment to the water column simulated during spring tides (60% of the annual export). The simulated resuspended MPB biomass is also higher during flood than ebb. Seventy-six percent of the annual export of MPB biomass from the sediment to the water column occurs during flood in the model. In the Bay of Bourgneuf (NW France), Gernez et al. (2017) also retrieved higher benthic Chl *a* resuspension in flood than in ebb using the remote sensing algorithm used in our study.

We compared the resuspended Chl *a* concentrations simulated for year 2012 with 2012 seawater Chl *a* concentrations remotely sensed above the mudflat and measured in situ at water quality monitoring stations in the vicinity of the Brouage mudflat. The simulated seasonal cycle of the resuspended MPB biomass is consistent with the winter, spring, and fall observations. The model suggests a higher contribution of benthic microalgae in winter-spring than in summer. Guarini et al. (2004) and Hernández Fariñas et al. (2017) analyzed the phytoplankton community in seawater sampled at water quality monitoring stations in the Bay of Marennes-Oléron and the Bay of Bourgneuf (160 km north of the Brouage mudflat), respectively. Both studies suggest a similar seasonal pattern with a higher contribution of benthic microalgae in seawater in winter-spring than in summer. Nevertheless, we remain cautious on the reasonable agreement between the model and in situ data as the number of in situ samples we used was defined by a threshold we set for benthic cells resuspension representativeness. Below 50% of benthic cells in the sample, the sample was discarded in the analysis. Such a threshold implies that, in summer, all the samples are discarded so no model-data comparison is possible. In addition, ~15 km separate the study site from the monitoring stations. Such a distance may involve some model-data discrepancies caused by grazing, MPB deposition, and resuspension occurring between sites.

The horizontal transport of the MPB cells within the water column may impact the biomass of resuspended MPB. Guarini et al. (2004) and Guarini et al. (2008) report an horizontal transport of resuspended MPB cells in the Bay of Marennes-Oléron and over the Brouage mudflat. In our modeling approach, there is no horizontal transport in seawater or deposition on the sea floor of the resuspended MPB biomass. Such a

parameterization implies that once resuspended, all the MPB biomass is definitely transported away from the study site. Similarly, the model precludes any incoming flux of MPB biomass produced in other areas and transported to the study site. Waves and current BSS can also shape the spatial distribution of *P. ulvae* individuals on the mudflat (Armonies & Hartke, 1995) and so the local grazing pressure on MPB developing in the sediment. In the model, the lack of grazing pressure on MPB cells resuspended in the water column may result into an overestimation of the simulated resuspended MPB biomass (Guizien et al., 2014). The intensive oyster farming in the Brouage mudflat vicinity can result into a substantial removal of the resuspended MPB biomass (Smaal & Zurburg, 1997). Such a process is not considered in the model. To that respect, an explicit benthopelagic coupling would be required to fully account for the complex biogeochemical processes controlling the planktonic activity within the water column (Hochard et al., 2012).

With respect to the rate and amplitude of the MPB resuspension, the simulated values compare with the values reported in the literature. The instantaneous resuspended MPB biomass simulated by the model reaches 110 mg Chl *a* m^{-3}, in the range of observations (~45 mg Chl *a* m^{-3} measured by Baillie & Welsh, 1980; 320 mg Chl *a* m^{-3}, derived from suspended particulate matter measurements by Koh et al., 2007; 52.5 mg Chl *a* m^{-3} retrieved from remote sensing data by Gernez et al., 2017). The maximum erosion rate of Chl *a* in the sediment simulated during massive resuspension events (8.93 mg Chl *a* m^{-2} hr^{-1} or 2.48 μg Chl *a* m^{-2} s^{-1}) is consistent with measurements (1.72 μg Chl *a* m^{-2} s^{-1}) made by Orvain et al. (2014) in July 2008 in an erosion flume with sediment samples gathered in the Brouage mudflat. In the model, the MPB biomass export to the water column through the fluff layer erosion corresponds to MPB resuspension without any concomitant sediment erosion. The chronic events of fluff layer erosion led to instantaneous resuspended Chl *a* concentrations between 0 and 5.51 mg Chl *a* m^{-2}. On the Brouage mudflat, Guarini et al. (2008) estimated the chronic resuspension to up to 11 mg Chl *a* m^{-3} in 1.5 m of seawater height (i.e., corresponding to 16.5 mg Chl *a* m^{-2}). They related it to a full resuspension of a well-established biofilm (~25 mg Chl *a* m^{-2}) rather than erosion of the fluff layer only. In the model, the export of the entire biofilm is represented through the massive resuspension.

4.2. Physical and Biological Controls on MPB Resuspension

4.2.1. Waves and Tides

On the annual scale, the simulated export of MPB biomass to the water column is partly driven by wave-related massive resuspension events. These events occur mostly in winter and, to a lesser extent, in fall. In the model, the high bottom wave orbital velocity in winter and fall results in high simulated values of τ_w and τ_{max}. On mudflats of the Ems estuary in The Netherlands, de Jonge and van Beusekom (1995) related the MPB resuspension to wind waves. They showed a concomitant increase of resuspended benthic Chl *a* concentration with an increase of wind speed. The Bay of Marennes-Oléron extends over 170 km^2 and, regarding the geometry of the Bay, the highest fetch in the area can established from the north-west or the south-west (Figure 1). This fetch configuration is promoted by dominant winds from the oceanic sector (SW to NW) especially during winter-fall (source: Meteo France 1961–1990). Such fetches drive wind waves with a short period and orbital motions that reach easily the shallow sea bottom with, as a result, the resuspension of the sediment including MPB biomass (Green & Coco, 2014). At the highest water depth simulated at our study site (3.24 m), orbital motions of waves with periods higher than 2 s start to interact with the sea bottom. Waves with periods higher than 2 s occur 55% of the time in 2012. As a consequence, orbital motions often reach the sea bottom in the model. Moreover, wave-related MPB resuspension in the Brouage mudflat is not only dominated by waves generated locally but also by swells entering in the Bay from the ocean (Bertin et al., 2005). As a result, and contrarily to de Jonge and van Beusekom (1995), the sediment and MPB resuspension are not related to local winds only as peaks of wave orbital velocity are not always associated to strong local winds. The low wave orbital velocity simulated in spring and summer results in a much lower contribution of massive resuspension events to MPB resuspension at these seasons.

With respect to tides, the tidal currents contribute to massive MPB resuspension events during spring tides. Only the highest current velocities reached during spring tides can overpass $\tau_{crit_{mass}}$. The high contribution of spring tides current velocity on sediment resuspension was suggested by Toublanc et al. (2016) in their 3-D modeling study in the Charente estuary in close vicinity of the Brouage mudflat. They suggest a higher concentration of resuspended sediment in spring tides than in neap tides, because the current velocity and τ_c were lower in neap tides.

Fourteen percent and 10% of the simulated events of MPB resuspension occurs at the flood beginning and at the end of ebb, respectively. The action of waves on sea bottom is limited by the water height (Figure 3). The wave height and orbital velocity increase with the water level until a critical depth when orbital motions at the bottom start to decrease (Green & Coco, 2014; Li et al., 2019; Mariotti & Fagherazzi, 2013). In the model, the average critical depth is about 1–1.25 m. Such a water height is reached mainly at the beginning and at the end of high tides, which explains the high simulated impact of average wave conditions on MPB resuspension at the beginning of flood and at the end of ebb. Moreover, the high current velocity and τ_c at the flood beginning and at the end of ebb, combine to high τ_w at this moment of the tide, which increases $\tau_{\max}$. Using a 2-D model, Le Hir et al. (2000) also simulated higher current velocities at the beginning of flood and at the end of ebb on the Brouage mudflat. Overall, the model reasonably simulates the process of MPB resuspension at both the tidal and seasonal scale.

4.2.2. MPB Behavior

The seasonal cycle of the MPB biomass in the sediment also plays a role in the seasonality of the massive MPB resuspension. Waves drive more frequent massive resuspension events in winter and fall. However, most of the high resuspension events (events identified when resuspended MPB biomass is higher than the last percentile of the resuspended MPB biomass simulated time series in 2012) are simulated in late winter-early spring. The occurrence from March to June of the simulated spring bloom of MPB biomass in the sediment explains this pattern. Because of the high MPB biomass in the sediment, the sediment erosion driven by strong-moderate hydrodynamical conditions leads to an important export of MPB biomass in the water column.

The mean time spent by MPB cells at the surface (γ) is a key parameter in the model that controls both the simulated MPB PP and resuspension. The highest value of instantaneous MPB resuspension is simulated when MPB cells remain longer at the sediment surface. The longer is the stay of the cells at the sediment surface, the higher is their PP. The MPB biomass accumulates in the sediment and leads to a high export of MPB biomass to the water column. In the model, the mean time spent by the MPB cells at the sediment surface is set according to the time required to induce photoinhibition (Blanchard et al., 2004). Combined with the MPB biomass in the sediment before the emersion period, γ sets the potential duration of the biofilm or the potential duration of the production period named γ* (hr) in the model. The longer is γ*, the higher is the PP and the more likely are the cells remaining at the surface resuspended during the rising tide.

Resuspension events also contribute to shape the dynamics of the MPB biomass in the sediment. For example, in early February and early and late March, the simulated MPB biomass in the sediment decreases in response to massive resuspension events. In the model, a minimum threshold of MPB biomass in the sediment (73 mg Chl a m^{-2}) is set when massive resuspension events occur. Such a threshold dampens the resuspension intensity when the MPB biomass is lower than this value. In their modeling study, Mariotti and Fagherazzi (2012) also set a constant background of MPB biomass during massive resuspension events to prevent any nonresilient behavior of the simulated MPB. In addition, the laboratory erosion flume experiments made by Valentine et al. (2014) suggest that only a small biofilm can build up when repeated erosion events occur.

In response to massive resuspension events, MPB inhabiting the sediment first centimeter can develop resilience strategies to maintain a background of active biomass in the sediment. Larson and Sundbäck (2008) suggested that MPB cells in anoxic stressful conditions could migrate down in the sediment and go into a dormant state and keep respiration demands to a minimum. The survival capacity of nonresting benthic diatoms can be due to heterotrophy on organic substrates present in the sediment (Tuchman et al., 2006). Veuger and van Oevelen (2011) suggested that nonresting benthic diatoms can remain in dark sediment for a year and remain fully photosynthetically active. Once the sediment uppermost layer is eroded, buried MPB cells from deeper sediment layers newly exposed to favorable growth conditions can get active and productive. MPB cells newly deposited on the eroded sediment can also initiate recolonization. In their field experiment, Pan et al. (2017) suggest that benthic diatoms are able to recolonize the sediment. By removing the top 2 cm of the microbial mat present at the sediment surface, the authors observed a rapid (4–7 days) recolonization by diatoms corresponding to epipelic groups triggered by the horizontal advection and redistribution of cells over the mudflat during high tides

4.2.3. Fauna

The chronic erosion of the fluff layer simulated by the model is responsible for a substantial export of the MPB biomass from the sediment to the water column in spring and summer. The Chl *a* content in the fluff

layer is fueled by the crawling activity of *P. ulvae* individuals, which increases the transfer of MPB biomass from the biofilm to the fluff layer. The high contribution of fluff layer erosion to total resuspended MPB biomass in spring and summer is driven by the relatively high *P. ulvae* density at these seasons. At the annual scale, the fluff layer erosion is more frequent than massive resuspension (31.3% and 24%, respectively). However, it contributes less to the total resuspended MPB biomass (36.7%) than massive resuspension events (63.3%). In our study, we considered the bioturbation by *P. ulvae* only but other fauna species can also contribute to bioturbation. On the upper Brouage mudflat, bivalve *Scrobicularia plana* individuals exhibit high densities (∼1,000 ind m^{-2}) and play an important role in the bioturbation process in this part of the mudflat (Orvain et al., 2007). Other abundant species of macrofauna and meiofauna (e.g., the homogeneously spatially distributed nematodes on the Brouage mudflat) can also bioturbate substantially the sediment (Passarelli et al., 2014; Rzeznik-Orignac et al., 2003). As we only explicitly account for the dominant MPB grazer at our study station, the model may underestimate bioturbation and the fluff layer erosion compared to the massive resuspension process.

The presence and grazing-crawling activity of *P. ulvae* can also impact the sediment bed roughness as the gastropod is able to cope with strong currents. Blanchard et al. (1997) and Orvain et al. (2003) suggest that the *P. ulvae* shell can increase the bed roughness, which results into an increase of the BSS. Such an effect is not represented in the model. However, the bed roughness variations driven by *P. ulvae* individuals might have a limited effect in the model as the simulated annual MPB PP and instantaneous resuspension show a low sensitivity to bed roughness.

4.2.4. Sediment

The instantaneous MPB resuspension and annual MPB PP simulated by the model are not sensitive to the bed roughness. The model is run with the same constant value used in Le Hir et al. (2000) in their 2-D hydrodynamical modeling study on the Brouage mudflat. Nevertheless, the Brouage mudflat is characterized by the presence of ridges and runnels (Gouleau et al., 2000), by the settlement of a sheet flow (i.e., a fluid sediment layer moving along the bottom) and the presence of biogenic structures. Consequently, the bed roughness is likely to vary in space and time. The horizontal resolution of the SCHISM physical model is ∼100 m on the Brouage mudflat, which is too coarse for resolving ridges and runnels. These morphological sea bed structures are important in the sediment erosion-deposition-consolidation mechanisms. Average wave conditions and tidal currents remobilize the sediment mainly in runnels (Carling et al., 2009). In contrast, strong wind waves and spring tides current and associated high BSS can induce sediment resuspension both in runnels and ridges (Carling et al., 2009; Fagherazzi & Mariotti, 2012). Blanchard et al. (2000) suggest that MPB colonize and consolidate preferentially ridges compared to runnels, which are more drainage structures. Consequently, ridges are more consolidated than runnels due to a high MPB and EPSs content (Blanchard et al., 2000). Marani et al. (2010) showed that biostabilization processes by halophytic vegetation and microbial biofilm is a key component of tidal morphological equilibrium. Therefore, even spatially distributed in patchiness, MPB might play a key role on the long- and short-term morphodynamic of the intertidal mudflat. The current and waves simulated by the SCHISM physical model compare with the ADCP measurements deployed in 2012 on a ridge of the Brouage mudflat, which suggests that the physical-biological model can reproduce the MPB dynamics prevailing on ridge-like structures.

In the model, the physical properties of the sediment are impacted by the biology. The sediment is consolidated by biota as the erosion threshold increases along with the MPB biomass in the sediment first centimeter. Such a mechanism represents the sediment consolidation by EPSs excreted mainly by MPB (Pierre et al., 2010; 2012). EPSs increase the adhesion of fine sediment grains (Decho, 1990, 2000) and decrease the sediment permeability, which results into a increase of the sediment consolidation (Zetsche et al., 2011). Consequently, the higher is the simulated MPB biomass in the sediment, the higher is simulated $\tau_{crit_{mass}}$. $\tau_{crit_{mass}}$ reaches a seasonal maximum in early May when the MPB biomass in the sediment is the highest. Pivato et al. (2019) described the relationship between the biostabilization effect and the seasonal cycle of MPB biomass as a positive feedback. The high MPB PP in spring promotes the fast recovery of MPB biomass in the sediment hence leading to a higher resistance to erosion through biostabilization. In that sense, MPB create their own favorable conditions for MPB biomass accumulation in the sediment in spring. On a mudflat in the Westerscheldt in The Netherlands, Stal (2010) reports the highest erosion threshold right after the MPB biomass maximum in the biofilm during one low tide. On a mudflat at Kjelst in the Danish Wadden Sea, Andersen (2001) also suggests a good correspondence between a well-established MPB biofilm and a high erosion threshold in spring and late summer-early winter. In our study, the simulated

seasonal maximum of $\tau_{crit_{mass}}$ (1.8 Pa) is sixfold higher than the critical BSS constant for bare cohesive sediment. This is consistent with the laboratory flume experiment of Neumeier et al. (2006) that suggests that biofilm-inhabited sediments exhibit a critical BSS fourfold to tenfold higher than in bare sediments without any established biofilm. On the Kapellebank mudflat of the Western Scheldt Estuary (the Netherlands), Zhu et al. (2019) also report a critical BSS fivefold higher in a sediment inhabited by diatoms than in sediments without diatoms. The erosion threshold commonly follows the Chl *a* content in sediment. However, a stronger correlation is found between sediment consolidation and EPSs production (Underwood & Paterson, 1993) by both benthic diatoms and bacterial assemblages (Chen et al., 2017), the latter process being not simulated by the model. Accounting for bacteria and EPSs production might improve the model ability to simulate the sediment consolidation.

4.3. MPB-Driven Benthic-Pelagic Flux

At the annual scale, 43% of the simulated PP is resuspended. In winter, the ratio between MPB resuspension and PP is the highest due to a moderate resuspension and a low PP. In contrast, in spring, the ratio decreases as resuspension reaches its seasonal maximum and PP is higher than in winter. With respect to secondary production, the simulated annual resuspension (60.8 g $C{\cdot}m^{-2}{\cdot}yr^{-1}$) is 1.3-fold higher than the annually integrated MPB ingestion by *P. ulvae* (41.1 g $C{\cdot}m^{-2}{\cdot}yr^{-1}$). It suggests that the export of MPB biomass to the water column is higher than the MPB grazing that builds up secondary production. Moreover, the simulated annual resuspension represents 33% of the phytoplankton PP estimated in the same study area (Struski & Bacher, 2006). Such a result highlights the key role played by MPB in the benthopelagic coupling. Using inverse modeling based on data from the Brouage mudflat, Saint-Béat et al. (2014) suggest that the export of particulate organic carbon from the benthic compartment fuels the pelagic carbon production when biofilm resuspension is considered in summer. MPB resuspension varies seasonally in response to contrasting hydrodynamical conditions. The coupled physical-biological model simulates such a seasonal dynamics that impacts the seasonal benthopelagic flux of organic carbon. This is not the case in Savelli et al. (2018), where MPB resuspension is formulated as a continuous and linear MPB loss term at high tide. Such a formulation in Savelli et al. (2018) results in a seasonality of resuspension that only varies according to the MPB biomass in the sediment without considering any physical forcing. It then implies that the higher is the MPB biomass in the sediment, the higher is the resuspension of the MPB biomass. Such a parametrization is not realistic considering the increase of sediment consolidation with the MPB biomass. In addition, this formulation might overestimate and underestimate the MPB resuspension during calm physical conditions and intense physical conditions, respectively.

5. Conclusion

We used a physical-biological model to assess the role of chronic and massive resuspension events on the MPB dynamics in a very productive temperate intertidal mudflat. The model reasonably simulates the seasonal pattern of MPB resuspension and gives some insights to our understanding of the contribution of the physical and biological mechanisms controlling the MPB export from the sediment to the water column:

- At the tidal scale, MPB resuspension is the highest in spring tides due to strong tidal currents. Over the year, 76% of the resuspended MPB biomass is exported to the water column at the flood beginning due to high velocity currents and low water heights that promote wave orbital motions-sea bottom interactions;
- In winter and fall, waves are the main driver for massive MPB resuspension events;
- During the spring bloom, MPB biomass accumulates and consolidates the sediment first centimeter. The simulated critical BSS is sixfold higher than the critical BSS constant for bare sediment;
- In spring, the density of *P. ulvae* individuals increases and so the bioturbation, which promotes MPB in the chronically eroded fluff layer at the sediment surface;
- When the MPB biomass in the sediment reaches its seasonal maximum in spring, massive resuspension events driven by the wave- and tidal-induced BSS and chronic fluff layer erosion events lead to the highest seasonal export of MPB biomass to the water column (from 1.1- to 3-fold higher than in other seasons in terms of Chl *a*). In terms of Chl *a*, massive and chronic resuspension events in spring represent 20% and 17.5% of the MPB biomass resuspended annually;
- In summer, MPB resuspension is the lowest (1.3- to 3-fold lower than in other seasons in terms of Chl *a*) due to calm hydrodynamical conditions and low MPB biomass in the sediment;
- At the annual scale, 43.3% of the MPB PP is resuspended to the water column and this export (60.8 g $C{\cdot}m^{-2}{\cdot}yr^{-1}$) exceeds the *P. ulvae* grazing pressure on MPB (41.1 g $C{\cdot}m^{-2}{\cdot}yr^{-1}$).

Accounting for the physically (tides and waves) and biologically (biostabilization and bioturbation) driven resuspension processes of MPB in predictive physical-biological coupled models is an important step in assessing the export of biogenic matter at the land-ocean interface. These processes could be represented into tri-dimensional (3-D) ocean-biogeochemical coupled models that resolve the 3-D fields of advection and diffusion in the water column required to simulate the spatial and temporal dynamics of MPB over a whole mudflat. Three-dimensional models would hence allow the assessment of benthopelagic MPB fluxes driven by the action of waves and tidal currents. Once in the water column, MPB can turn into a planktonic life forms whose growth rate can depend on seawater nutrients, light availability, and temperature (MacIntyre et al., 1996). According to the prevailing environmental conditions, MPB can be grazed, contribute to pelagic PP (Guarini et al., 2008; Polsenaere et al., 2012), remain into the water column until senescence or can sink and return to a benthic life form (Guizien et al., 2014; MacIntyre et al., 1996; Miller et al., 1996). Such processes could be inferred by coupling MPB models that include the resuspension mechanisms with high-resolution regional models that simulate the interactions between the coastal ocean and the planktonic ecosystem dynamics. Accounting for such processes in the carbon budget of the land-ocean interface would improve our understanding and assessment of the benthopelagic fluxes of organic matter and bring new insights on the role played by MPB in the carbon cycle of the global coastal ocean.

Acknowledgments
This research was funded by the Centre national d'études spatiales (CNES), the Centre National de la Recherche Scientifique (CNRS, LEFE-EC2CO program), the Région Nouvelle-Aquitaine and the European Union (CPER/FEDER), and the Groupement d'Intérêt Public (GIP) Seine-Aval PHARESEE project. R. S. was supported by a PhD fellowship from the French Ministry of Higher Education, Research and Innovation. The authors acknowledge Meteo France for providing meteorological data and the Institut National de l'Information Géographique et Forestière (IGN) and the Service Hydrographique et Océanographique de la Marine (SHOM) for providing the digital elevation model of Charente Maritime LITTO3D®. This research is part of fulfillment of the requirements for a PhD degree (RS) at the Université de La Rochelle, France. P. G. acknowledges the support of the BIO-Tide project, funded through the 2015–2016 BiodivERsA COFUND call for research proposals, with the national funders BelSPO, FWO, ANR, and SNSF. Air temperature, relative humidity, and shortwave radiations from LA ROCHELLE (LA ROCHELLE-ILE DE RE) Meteo France weather station (Code 17300009) are available at https://publitheque.meteo.fr in exchange of money credits. Sea level atmospheric pressure and wind velocity were extracted from the atmospheric reanalysis CFSR (NCEP Climate Forecast System Version 2 [CFSv2] selected hourly time series products, https://rda.ucar165.edu/datasets/ds094.1). MERIS Level2 full-resolution 300-m images are available for download from the ESAs MERCI server (https://merisfrs-merci-ds.eo.esa.int/). REPHY water quality monitoring and phytoplankton taxonomic data are available at the website (https://www.seanoe.org/data/00361/47248/). Several chapters of R. S.'s PhD thesis will use the model presented in this study. As a consequence, the model presented in this study was archived in a ZENODO repository (http://doi.org/10.5281/zenodo.3274396), which will be available after an embargo period corresponding to the completion of this PhD thesis (December 2020). The ADCP measurements, the input/output files of the model are all available in the same repository (http://doi.org/10.5281/zenodo.3274396). The authors also thank two anonymous reviewers for valuable comments on the paper.

References

Andersen, T. (2001). Seasonal variation in erodibility of two temperate, microtidal mudflats. *Estuarine, Coastal and Shelf Science*, *53*(1), 1–12.

Andersen, T. J., Fredsoe, J., & Pejrup, M. (2007). In situ estimation of erosion and deposition thresholds by Acoustic Doppler Velocimeter (ADV). *Estuarine, Coastal and Shelf Science*, *75*(3), 327–336.

Ariathurai, R., & Krone, R. B. (1976). Finite element model for cohesive sediment transport. *Journal of the Hydraulics Division*, *102*(3), 323–338.

Armonies, W., & Hartke, D. (1995). Floating of mud snails Hydrobia ulvae in tidal waters of the Wadden Sea, and its implications in distribution patterns. *Helgoländer Meeresuntersuchungen*, *49*(1), 529.

Austen, I., Andersen, T. J., & Edelvang, K. (1999). The influence of benthic diatoms and invertebrates on the erodibility of an intertidal mudflat, the Danish Wadden Sea. *Estuarine, Coastal and Shelf Science*, *49*(1), 99–111.

Baillie, P. W., & Welsh, B. L. (1980). The effect of tidal resuspension on the distribution of intertidal epipelic algae in an estuary. *Estuarine and Coastal Marine Science*, *10*(2), 165–180.

Barranguet, C., Kromkamp, J. C., & Peene, J. (1998). Factors controlling primary production and photosynthetic characteristics of intertidal microphytobenthos. *Marine Ecology Progress Series*, *173*, 117–126

Bassoullet, P., Le Hir, P., Gouleau, D., & Robert, S. (2000). Sediment transport over an intertidal mudflat: Field investigations and estimation of fluxes within the "Baie de Marennes-Oléron"(France). *Continental shelf research*, *20*(12-13), 1635–1653.

Battjes, J. A., & Janssen, J. (1978). Energy loss and set-up due to breaking of random waves. *Coastal Engineering Proceedings*, *1*(16), 32.

Belin, C., & Raffin, B. (1990). REPHY (Réseau de suivi du phytoplancton): Inventaire cartographique des points de prélévements (1990), *Technical document*. Retrieved from https://archimer.ifremer.fr/doc/00174/28523/

Benyoucef, I., Blandin, E., Lerouxel, A., Jesus, B., Rosa, P., Méléder, V., et al. (2014). Microphytobenthos interannual variations in a north-European estuary (Loire estuary, France) detected by visible-infrared multispectral remote sensing. *Estuarine Coastal and Shelf Science*, *136*, 43–52.

Bertin, X., Bruneau, N., Breilh, J.-F., Fortunato, A. B., & Karpytchev, M. (2012). Importance of wave age and resonance in storm surges: The case xynthia, bay of biscay. *Ocean Modelling*, *42*, 16–30.

Bertin, X., Chaumillon, E., Sottolichio, A., & Pedreros, R. (2005). Tidal inlet response to sediment infilling of the associated bay and possible implications of human activities: The Marennes-Oléron Bay and the Maumusson Inlet, France. *Continental Shelf Research*, *25*(9), 1115–1131.

Bidlot, J.-R., Janssen, P., & Abdalla, S. (2007). A revised formulation of ocean wave dissipation and its model impact, *Tech. Memo.*, 509.

Blanchard, G., Agion, T., Guarini, J.-M., Herlory, O., & Richard, P. (2006). Analysis of the short-term dynamics of microphytobenthos biomass on intertidal mudflats. *Verhandelingen van de Koninklijke Nederlandse Akademie van Wetenschappen-Natuurkunde-Ser*, *2*(103), 85–98.

Blanchard, G. F., Guarini, J.-M., Dang, C., & Richard, P. (2004). Characterizing and quantifying photoinhibition in intertidal microphytobenthos. *Journal of phycology*, *40*(4), 692–696.

Blanchard, G. F., Paterson, D. M., Stal, L. J., Richard, P., Galois, R., Huet, V., et al. (2000). The effect of geomorphological structures on potential biostabilisation by microphytobenthos on intertidal mudflats. *Continental Shelf Research*, *20*(10), 1243–1256.

Blanchard, G., Sauriau, P., Cariou-Le Gall, V., Gouleau, D., Garet, M., & Olivier, F. (1997). Kinetics of tidal resuspension of microbiota: Testing the effects of sediment cohesiveness and bioturbation using flume experiments. *Marine Ecology Progress Series*, *151*, 17–25.

Blanchard, G., Simon-Bouhet, B., & Guarini, J.-M. (2002). Properties of the dynamics of intertidal microphytobenthic biomass. *Journal of the Marine Biological Association of the United Kingdom*, *82*(6), 1027–1028.

Bocher, P., Piersma, T., Dekinga, A., Kraan, C., Yates, M. G., Guyot, T., et al. (2007). Site-and species-specific distribution patterns of molluscs at five intertidal soft-sediment areas in northwest Europe during a single winter. *Marine Biology*, *151*(2), 577–594.

Brito, A. C., Benyoucef, I., Jesus, B., Brotas, V., Gernez, P., Mendes, C. R., et al. (2013). Seasonality of microphytobenthos revealed by remote sensing in a South European estuary. *Continental Shelf Research*, *66*, 83–91.

Carling, P., Williams, J., Croudace, I., & Amos, C. (2009). Formation of mud ridge and runnels in the intertidal zone of the Severn Estuary, UK. *Continental Shelf Research*, *29*(16), 1913–1926.

Carlton, J. T., & Hodder, J. (2003). Maritime mammals: Terrestrial mammals as consumers in marine intertidal communities. *Marine Ecology Progress Series*, *256*, 271–286.

Cartaxana, P., Domingues, N., Cruz, S., Jesus, B., Laviale, M., Serôdio, J, & da Silva, J. M. (2013). Photoinhibition in benthic diatom assemblages under light stress. *Aquatic Microbial Ecology*, *70*(1), 87–92.

Cartaxana, P., Vieira, S., Ribeiro, L., Rocha, R. J., Cruz, S., Calado, R., & da Silva, J. M. (2015). Effects of elevated temperature and CO_2 on intertidal microphytobenthos. *BMC ecology*, *15*(1), 10.

Chen, X., Zhang, C., Zhou, Z., Gong, Z., Zhou, J., Tao, J., et al. (2017). Stabilizing effects of bacterial biofilms: EPS penetration and redistribution of bed stability down the sediment profile. *Journal of Geophysical Research: Biogeosciences*, *122*, 3113–3125. https://doi.org/10.1002/2017JG004050

Christie, M., Dyer, K., & Turner, P. (1999). Sediment flux and bed level measurements from a macrotidal mudflat. *Estuarine, Coastal and Shelf Science*, *49*(5), 667–688.

Daggers, T. D., Kromkamp, J. C., Herman, P. M., & van der Wal, D. (2018). A model to assess microphytobenthic primary production in tidal systems using satellite remote sensing. *Remote Sensing of Environment*, *211*, 129–145.

Davis, W. R. (1993). The role of bioturbation in sediment resuspension and its interaction with physical shearing. *Journal of Experimental Marine Biology and Ecology*, *171*(2), 187–200.

de Jonge, V. N., & van Beusekom, J. E. E. (1992). Contribution of resuspended microphytobenthos to total phytoplankton in the EMS estuary and its possible role for grazers. *Netherlands Journal of Sea Research*, *30*(C), 91–105.

de Jonge, V. N., & van Beusekom, J. E. E. (1995). Wind-and tide-induced resuspension of sediment and microphytobenthos from tidal flats in the Ems estuary. *Limnology and oceanography*, *40*(4), 776–778.

Decho, A. W. (1990). Microbial exopolymer secretions in ocean environments: Their role(s) in food webs and marine processes. *Oceanography and Marine Biology*, *28*(737153), 9–16.

Decho, A. W. (2000). Microbial biofilms in intertidal systems: An overview. *Continental shelf research*, *20*(10-11), 1257–1273.

Dupuy, C., Mallet, C., Guizien, K., Montanié, H., Bréret, M., Mornet, F., et al. (2014). Sequential resuspension of biofilm components (viruses, prokaryotes and protists) as measured by erodimetry experiments in the Brouage mudflat (French Atlantic coast). *Journal of Sea Research*, *92*, 56–65.

Echappé, C., Gernez, P., Méléder, V., Jesus, B., Cognie, B., Decottignies, P., et al. (2018). Satellite remote sensing reveals a positive impact of living oyster reefs on microalgal biofilm development. *Biogeosciences*, *15*(3), 905–918.

Fagherazzi, S., & Mariotti, G. (2012). Mudflat runnels: Evidence and importance of very shallow flows in intertidal morphodynamics. *Geophysical Research Letters*, *39*, L14402. https://doi.org/10.1029/2012GL052542

French, J. R., Burningham, H., & Benson, T. (2008). Tidal and meteorological forcing of suspended sediment flux in a muddy mesotidal estuary. *Estuaries and Coasts*, *31*(5), 843.

French Observation and Monitoring program for Phytoplankton and Hydrology in coastal waters (2017). REPHY dataset—French Observation and Monitoring program for Phytoplankton and Hydrology in coastal waters. 1987-2016 Metropolitan data. [Dataset] Retrieved from https://www.seanoe.org/data/00361/47248/

Galván, K., Fleeger, J. W., & Fry, B. (2008). Stable isotope addition reveals dietary importance of phytoplankton and microphytobenthos to saltmarsh infauna. *Marine Ecology Progress Series*, *359*, 37–49.

Gernez, P., Doxaran, D., & Barillé, L. (2017). Shellfish aquaculture from space: Potential of Sentinel2 to monitor tide-driven changes in turbidity, chlorophyll concentration and oyster physiological response at the scale of an oyster farm. *Frontiers in Marine Science*, *4*, 137.

Gons, H. J. (1999). Optical teledetection of chlorophyll a in turbid inland waters. *Environmental Science & Technology*, *7*, 1127–1132.

Gons, H. J., Rijkeboer, M., & Ruddick, K. G. (2005). Effect of a waveband shift on chlorophyll retrieval from MERIS imagery of inland and coastal waters. *Journal of Plankton research*, *27*(1), 125–127.

Gouleau, D., Jouanneau, J.-M., Weber, O., & Sauriau, P.-G. (2000). Short-and long-term sedimentation on Montportail–Brouage intertidal mudflat, Marennes–Oleron Bay (France). *Continental Shelf Research*, *20*(12-13), 1513–1530.

Green, M. O., & Coco, G. (2014). Review of wave-driven sediment resuspension and transport in estuaries. *Reviews of Geophysics*, *52*, 77–117. https://doi.org/10.1002/2013rg000437

Guarini, J.-M., Blanchard, G., Bacher, C., Gros, P., Riera, P., Richard, P., et al. (1998). Dynamics of spatial patterns of microphytobenthic biomass: Inferences from a geostatistical analysis of two comprehensive surveys in Marennes-Oléron Bay (France). *Marine Ecology Progress Series*, *166*, 131–141.

Guarini, J.-M., Blanchard, G., Gros, P., Gouleau, D., & Bacher, C. (2000). Dynamic model of the short-term variability of microphytobenthic biomass on temperate intertidal mudflats. *Marine Ecology Progress Series*, *195*, 291–303.

Guarini, J.-M., Gros, P., Blanchard, G., Richard, P., & Fillon, A. (2004). Benthic contribution to pelagic microalgal communities in two semi-enclosed European-type littoral ecosystems (Marennes-Oléron Bay and Aiguillon Bay, France). *Journal of Sea Research*, *52*(4), 241–258.

Guarini, J.-M., Sari, N., & Moritz, C. (2008). Modelling the dynamics of the microalgal biomass in semi-enclosed shallow-water ecosystems. *Ecological Modelling*, *211*(3-4), 267–278.

Guizien, K., Dupuy, C., Ory, P., Montanié, H., Hartmann, H., Chatelain, M., & Karpytchev, M. (2014). Microorganism dynamics during a rising tide: Disentangling effects of resuspension and mixing with offshore waters above an intertidal mudflat. *Journal of Marine Systems*, *129*, 178–188.

Hammersley, J., & Handscomb, D. (1964). *Monte Carlo methods*. London: Methuen & Co. Ltd.

Hasselmann, K., Barnett, T., Bouws, E., Carlson, H., Cartwright, D., Enke, K., et al. (1973). Measurements of wind-wave growth and swell decay during the Joint North Sea Wave Project (JONSWAP). *Ergänzungsheft*, *12*(8), 1–95.

Hasselmann, S., Hasselmann, K., Allender, J., & Barnett, T. (1985). Computations and parameterizations of the nonlinear energy transfer in a gravity-wave spectrum. Part II: Parameterizations of the nonlinear energy transfer for application in wave models. *Journal of Physical Oceanography*, *15*(11 , Nov. 1985), 1378–1391.

Healy, T., Wang, Y., & Healy, J.-A. (2002). *Muddy coasts of the world: Processes, deposits and function*, vol. 4: Elsevier.

Herlory, O., Guarini, J.-M., Richard, P., & Blanchard, G. (2004). Microstructure of microphytobenthic biofilm and its spatio-temporal dynamics in an intertidal mudflat (Aiguillon Bay, France). *Marine Ecology Progress Series*, *282*, 33–44.

Herman, P. M. J., Middelburg, J. J., Widdows, J., Lucas, C. H., & Heip, C. H. R. (2000). Stable isotopes as trophic tracers: Combining field sampling and manipulative labelling of food resources for macrobenthos. *Marine Ecology Progress Series*, *204*, 79–92.

Hernández Fariñas, T., Ribeiro, L., Soudant, D., Belin, C., Bacher, C., Lampert, L., & Barillé, L. (2017). Contribution of benthic microalgae to the temporal variation in phytoplankton assemblages in a macrotidal system. *Journal of Phycology*, *53*(5), 1020–1034.

Hochard, S., Pinazo, C., Rochelle-Newall, E., & Pringault, O. (2012). Benthic pelagic coupling in a shallow oligotrophic ecosystem: Importance of microphytobenthos and physical forcing. *Ecological modelling*, *247*, 307–318.

Jardine, C. B., Bond, A. L., Davidson, P. J., Butler, R. W., & Kuwae, T. (2015). Biofilm consumption and variable diet composition of Western Sandpipers (Calidris mauri) during migratory stopover. *PloS one*, *10*(4), e0124164.

Kang, C., Lee, Y., Eun, J. C., Shin, J., Seo, I., & Hong, J. (2006). Microphytobenthos seasonality determines growth and reproduction in intertidal bivalves. *Marine Ecology Progress Series*, *315*, 113–127.

Ke, X., Collins, M., & Poulos, S. (1994). Velocity structure and sea bed roughness associated with intertidal (sand and mud) flats and saltmarshes of the wash, uk. *Journal of Coastal Research*, *10*(3), 702–715.

Kervella, S. (2009). Dynamique des sédiments fins et mixtes des zones intertidales de la baie de Marennes-Oléron: Caractérisation des sédiments, processus hydro-sédimentaires et modélisation appliquée (Unpublished doctoral dissertation), La Rochelle.

Koh, C.-H., Khim, J. S., Araki, H., Yamanishi, H., & Koga, K. (2007). Within day and seasonal patterns of microphytobenthos biomass determined by co-measurement of sediment and water column chlorophylls in the intertidal mud at of Nanaura, Saga, Ariake Sea, Japan. *Estuarine, Coastal and Shelf Science*, *72*(1-2), 42–52.

Koh, C.-H., Khim, J. S., Araki, H., Yamanishi, H., Mogi, H., & Koga, K. (2006). Tidal resuspension of microphytobenthic chlorophyll a in a Nanaura mudflat, Saga, Ariake Sea, Japan: Flood-ebb and spring-neap variations. *Marine Ecology Progress Series*, *312*, 85–100.

Komen, G. J., Cavaleri, L., Donelan, M., Hasselmann, K., Hasselmann, S., & Janssen, P. (1996). *Dynamics and modelling of ocean waves*: Cambridge university press.

Krumme, U., Keuthen, H., Barletta, M., Saint-Paul, U., & Villwock, W. (2008). Resuspended intertidal microphytobenthos as major diet component of planktivorous Atlantic anchoveta Cetengraulis edentulus (Engraulidae) from equatorial mangrove creeks. *Ecotropica*, *14*, 121–128.

Larson, F., & Sundbäck, K. (2008). Role of microphytobenthos in recovery of functions in a shallow-water sediment system after hypoxic events. *Marine Ecology Progress Series*, *357*, 1–16.

Le Hir, P., Monbet, Y., & Orvain, F. (2007). Sediment erodability in sediment transport modelling: Can we account for biota effects? *Continental Shelf Research*, *27*(8), 1116–1142.

Le Hir, P., Roberts, W., Cazaillet, O., Christie, M., Bassoullet, P., & Bacher, C. (2000). Characterization of intertidal flat hydrodynamics. *Continental shelf research*, *20*(12-13), 1433–1459.

Leroux, S. (1956). Phytoplancton et contenus stomacaux d'huîtres portugaises (Gryphea angulata Lmk) dans le bassin d'Arcachon. *Rev Trav Inst Pêches Marit*, *20*(2), 163–170.

Li, X., Leonardi, N., & Plater, A. J. (2019). Wave-driven sediment resuspension and salt marsh frontal erosion alter the export of sediments from macro-tidal estuaries. *Geomorphology*, *325*, 17–28.

Longuet-Higgins, M. S., & Stewart, R. (1964). Radiation stresses in water waves; A physical discussion, with applications, *Deep sea research and oceanographic abstracts* (vol. 11, pp. 529–562): Elsevier.

Lucas, C. H., Banham, C., & Holligan, P. M. (2001). Benthic-pelagic exchange of microalgae at a tidal flat. 2. Taxonomic analysis. *Marine Ecology Progress Series*, *212*, 39–52.

Luna-Acosta, A., Budzinski, H., Le Menach, K., Thomas-Guyon, H., & Bustamante, P. (2015). Persistent organic pollutants in a marine bivalve on the marennes-oléron bay and the gironde estuary (french atlantic coast)part 1: Bioaccumulation. *Science of The Total Environment*, *514*, 500–510.

MacIntyre, H. L., Geider, R. J., & Miller, D. C. (1996). Microphytobenthos: The ecological role of the "secret garden" of unvegetated, shallow-water marine habitats. I. Distribution, abundance and primary production. *Estuaries*, *19*(2), 186–201.

Madsen, K. N., Nilsson, P., & Sundbäck, K. (1993). The influence of benthic microalgae on the stability of a subtidal sediment. *Journal of Experimental Marine Biology and Ecology*, *170*(2), 159–177.

Marani, M., D'Alpaos, A., Lanzoni, S., Carniello, L., & Rinaldo, A. (2010). The importance of being coupled: Stable states and catastrophic shifts in tidal biomorphodynamics. *Journal of Geophysical Research*, *115*, F04004. https://doi.org/10.1029/2009JF001600

Mariotti, G., & Fagherazzi, S. (2012). Modeling the effect of tides and waves on benthic biofilms. *Journal of Geophysical Research*, *117*, G04010. https://doi.org/10.1029/2012JG002064

Mariotti, G., & Fagherazzi, S. (2013). Wind waves on a mudflat: The influence of fetch and depth on bed shear stresses. *Continental Shelf Research*, *60*, S99–S110.

Mehta, A. J., Hayter, E. J., Parker, W. R., Krone, R. B., & Teeter, A. M. (1989). Cohesive sediment transport. I: Process description. *Journal of Hydraulic Engineering*, *115*(8), 1076–1093.

Méléder, V., Jesus, B., Barnett, A., Barillé, L., & Lavaud, J. (2018). Microphytobthos primary production estimated by hyperspectral reflectance. *PloS One*, *13*(5), e0197093.

Mengual, B., Hir, P., Cayocca, F., & Garlan, T. (2017). Modelling fine sediment dynamics: Towards a common erosion law for fine sand, mud and mixtures. *Water*, *9*(8), 564.

Millenium Ecosystem Assessment (2005). *Ecosystems and human well-being: Synthesis*: Island press Washington, DC.

Miller, D. C., Geider, R. J., & MacIntyre, H. L. (1996). Microphytobenthos: The ecological role of the "secret garden" of unvegetated, shallow-water marine habitats. II. Role in sediment stability and shallow-water food webs. *Estuaries*, *19*(2), 202–212.

Neumeier, U., Lucas, C. H., & Collins, M. (2006). Erodibility and erosion patterns of mudflat sediments investigated using an annular flume. *Aquatic Ecology*, *40*(4), 543–554. https://doi.org/10.1007/s10452-004-0189-8

Newell, C., Shumway, S., Cucci, T., & Selvin, R. (1989). The effects of natural seston particle size and type on feeding rates, feeding selectivity and food resource availability for the mussel Mytilus edulis Linnaeus, 1758 at bottom culture sites in Maine. *Journal Shellfish Research*, *8*(1), 187–196.

Orvain, F., Guizien, K., Lefebvre, S., Bréret, M., & Dupuy, C. (2014). Relevance of macrozoobenthic grazers to understand the dynamic behaviour of sediment erodibility and microphytobenthos resuspension in sunny summer conditions. *Journal of Sea Research*, *92*, 46–55.

Orvain, F., Le Hir, P., & Sauriau, P.-G. (2003). A model of fluff layer erosion and subsequent bed erosion in the presence of the bioturbator, Hydrobia ulvae. *Journal of Marine Research*, *61*(6), 821–849.

Orvain, F., Sauriau, P.-G., Le Hir, P., Guillou, G., Cann, P., & Paillard, M. (2007). Spatio-temporal variations in intertidal mudflat erodability: Marennes-Oléron Bay, western France. *Continental Shelf Research*, *27*(8), 1153–1173.

Orvain, F., Sauriau, P.-G., Sygut, A., Joassard, L., & Le Hir, P. (2004). Interacting effects of Hydrobia ulvae bioturbation and microphytobenthos on the erodibility of mudflat sediments. *Marine Ecology Progress Series*, *278*, 205–223.

Pan, J., Cuadrado, D. G., & Bournod, C. N. (2017). Diatom-driven recolonization of microbial mat-dominated siliciclastic tidal at sediments. *FEMS Microbiology Ecology*, *93*(10), 1–3.

Partheniades, E. (1962). *A study of erosion and deposition of cohesive soils in salt water*. Berkeley: University of California.

Passarelli, C., Olivier, F., Paterson, D. M., Meziane, T., & Hubas, C. (2014). Organisms as cooperative ecosystem engineers in intertidal flats. *Journal of Sea Research*, *92*, 92–101.

Paterson, D. M. (1989). Short-term changes in the erodibility of intertidal cohesive sediments related to the migratory behavior of epipelic diatoms. *Limnology and Oceanography*, *34*(1), 223–234.

Paulmier, G. (1972). Seston, phytoplancton et microphytobenthos en rivière d'Auray: leur rôle dans le cycle biologique des huitres Ostrea edulis L (Unpublished doctoral dissertation).
Perissinotto, R., Nozais, C., Kibirige, I., & Anandraj, A. (2003). Planktonic food webs and benthic-pelagic coupling in three South African temporarily-open estuaries. *Acta Oecologica*, *24*, 307–316.
Perkins, R. G., Lavaud, J., Serôdio, J., Mouget, J.-L., Cartaxana, P., Rosa, P., et al. (2010). Vertical cell movement is a primary response of intertidal benthic biofilms to increasing light dose. *Marine Ecology Progress Series*, *416*, 93–103.
Pierre, G., Graber, M., Orvain, F., Dupuy, C., & Maugard, T. (2010). Biochemical characterization of extracellular polymeric substances extracted from an intertidal mudflat using a cation exchange resin. *Biochemical Systematics and Ecology*, *38*(5), 917–923.
Pierre, G., Graber, M., Rafiliposon, B. A., Dupuy, C., Orvain, F., De Crignis, M., & Maugard, T. (2012). Biochemical composition and changes of Extracellular Polysaccharides (ECPS) produced during microphytobenthic biofilm development (Marennes-Oléron, France). *Microbial Ecology*, *63*(1), 157–169.
Pivato, M., Carniello, L., Moro, I., & D'Odorico, P. (2019). On the feedback between water turbidity and microphytobenthos growth in shallow tidal environments. *Earth Surface Processes and Landforms*, *44*(5), 1192–1206.
Polsenaere, P., Lamaud, E., Lafon, V., Bonnefond, J.-M., Bretel, P., Delille, B., et al. (2012). Spatial and temporal CO_2 exchanges measured by Eddy Covariance ver a temperate intertidal flat and their relationships to net ecosystem roduction. *Biogeosciences*, *1*, 249–268.
Rast, M., Bezy, J., & Bruzzi, S. (1999). The ESA Medium Resolution Imaging Spectrometer MERIS a review of the instrument and its mission. *International Journal of Remote Sensing*, *20*(9), 1681–1702.
Roland, A., Zhang, Y. J., Wang, H. V., Meng, Y., Teng, Y.-C., Maderich, V., et al. (2012). A fully coupled 3D wave-current interaction model on unstructured grids. *Journal of Geophysical Research*, *117*, C00J33. https://doi.org/10.1029/2012jc007952
Rzeznik-Orignac, J., Fichet, D., & Boucher, G. (2003). Spatio-temporal structure of the nematode assemblages of the Brouage mudflat (Marennes Oléron, France). *Estuarine, Coastal and Shelf Science*, *58*(1), 77–88.
Saint-Béat, B., Dupuy, C., Agogué, H., Carpentier, A., Chalumeau, J., Como, S., et al. (2014). How does the resuspension of the biofilm alter the functioning of the benthospelagos coupled food web of a bare mud at in marennes-oléron bay (ne atlantic)? *Journal of Sea Research*, *92*, 144–157. https://doi.org/10.1016/j.seares.2014.02.003
Saint-Béat, B., Dupuy, C., Bocher, P., Chalumeau, J., De Crignis, M., Fontaine, C., et al. (2013). Key features of intertidal food webs that support migratory shorebirds. *PLoS One*, *8*(10), e76739.
Savelli, R., Dupuy, C., Barillé, L., Lerouxel, A., Guizien, K., Philippe, A., et al. (2018). On biotic and abiotic drivers of the microphytobenthos seasonal cycle in a temperate intertidal mudflat: A modelling study. *Biogeosciences*, *15*(23), 7243–7271.
Schlichting, H., & Gersten, K. (2016). *Boundary-layer theory*: Springer.
Smaal, A. C., & Zurburg, W. (1997). The uptake and release of suspended and dissolved material by oysters and mussels in Marennes-Oleron Bay. *Aquatic Living Resources*, *10*(1), 23–30.
Soletchnik, P., Faury, N., Razet, D., & Goulletquer, P. (1998). Hydrobiology of the Marennes-Oléron Bay. Seasonal indices and analysis of trends from 1978 to 1995. *Hydrobiologia*, *386*, 131–146.
Soletchnik, P., Le Moine, O., & Polsenaere, P. (2017). Evolution de l'environnement hydroclimatique du bassin de Marennes-Oléron dans le contexte du changement global, *Scientific report*. Retrieved from https://archimer.ifremer.fr/doc/00387/49815/
Soletchnik, P., Polsenaere, P., & Le Moine, O. (2018). Effet du changement global sur la biologie de l'huître creuse (C. gigas) dans le Bassin de Marennes-Oléron. Résultats, hypothéses et discussion, *Scientific report*. Retrieved from https://archimer.ifremer.fr/doc/00441/55239/
Soulsby, R. (1997). Dynamics of marine sands: A manual for practical applications. Thomas Telford.
Stal, L. J. (2010). Microphytobenthos as a biogeomorphological force in intertidal sediment stabilization. *Ecological Engineering*, *36*(2), 236–245.
Struski, C., & Bacher, C. (2006). Preliminary estimate of primary production by phytoplankton in Marennes-Oléron Bay, France. *Estuarine, Coastal and Shelf Science*, *66*(1-2), 323–334.
Swart, D. H. (1974). Offshore sediment transport and equilibrium beach profiles, Delft University of Technology, TU Delft.
Toublanc, F., Brenon, I., & Coulombier, T. (2016). Formation and structure of the turbidity maximum in the macrotidal Charente estuary (France): Influence of fluvial and tidal forcing. *Estuarine, Coastal and Shelf Science*, *169*, 1–14.
Tuchman, N. C., Schollett, M. A., Rier, S. T., & Geddes, P. (2006). Differential heterotrophic utilization of organic compounds by diatoms and bacteria under light and dark conditions, *Advances in algal biology: A commemoration of the work of Rex Lowe* (pp. 167–177): Springer.
Ubertini, M., Lefebvre, S., Gangnery, A., Grangeré, K., Le Gendre, R., & Orvain, F. (2012). Spatial variability of benthic-pelagic coupling in an estuary ecosystem: Consequences for microphytobenthos resuspension phenomenon. *PloS one*, *7*(8), e44155.
Underwood, G. J. C. (2001). Microphytobenthos, (Second Edition). In J. H. Steele (Ed.), *Encyclopedia of ocean sciences (second edition)* (pp. 807–814). Oxford: Academic Press.
Underwood, G. J. C., & Kromkamp, J. (1999). Primary production by phytoplankton and microphytobenthos in estuaries, *Advances in ecological research* (pp. 93–153): Elsevier.
Underwood, G. J. C., & Paterson, D. M. (1993). Seasonal changes in diatom biomass, sediment stability and biogenic stabilization in the Severn Estuary. *Journal of the Marine Biological Association of the United Kingdom*, *73*(4), 871–887.
Valentine, K., Mariotti, G., & Fagherazzi, S. (2014). Repeated erosion of cohesive sediments with biofilms. *Advances in Geosciences*, *39*, 9–14.
van der Wal, D., Wielemaker-van den Dool, A., & Herman, P. M. (2010). Spatial synchrony in intertidal benthic algal biomass in temperate coastal and estuarine ecosystems. *Ecosystems*, *13*(2), 338–351.
Verney, R., Brun-Cottan, J.-C., Lafite, R., Deloffre, J., & Taylor, J. (2006). Tidally induced shear stress variability above intertidal mudflats in the macrotidal Seine estuary. *Estuaries and Coasts*, *29*(4), 653–664.
Veuger, B., & van Oevelen, D. (2011). Long-term pigment dynamics and diatom survival in dark sediment. *Limnology and Oceanography*, *56*(3), 1065–1074.
Vieira, S., Ribeiro, L., da Silva, J. M., & Cartaxana, P. (2013). Effects of short-term changes in sediment temperature on the photosynthesis of two intertidal microphytobenthos communities. *Estuarine, Coastal and Shelf Science*, *119*, 112–118.
Willows, R. I., Widdows, J., & Wood, R. (1998). Influence of an infaunal bivalve on the erosion of an intertidal cohesive sediment: A flume and modeling study. *Limnology and Oceanography*, *43*(6), 1332–1343.
Wiltshire, K. H., Tolhurst, T., Paterson, D. M., Davidson, I., & Gust, G. (1998). Pigment fingerprints as markers of erosion and changes in cohesive sediment surface properties in simulated and natural erosion events. *Geological Society, London, Special Publications*, *139*(1), 99–114. https://doi.org/10.1144/GSL.SP.1998.139.01.08
Zetsche, E., Paterson, D., Lumsdon, D., & Witte, U. (2011). Temporal variation in the sediment permeability of an intertidal sandflat. *Marine Ecology Progress Series*, *441*, 49–63.
Zhang, Y. J., Ye, F., Stanev, E. V., & Grashorn, S. (2016). Seamless cross-scale modeling with SCHISM. *Ocean Modelling*, *102*, 64–81.
Zhu, Q., van Prooijen, B., Maan, D., Wang, Z., Yao, P., Daggers, T., & Yang, S. (2019). *Geomorphology*, *345*, 345.

Erratum

In the originally published version of this article, Vincent Le Fouest was erroneously omitted from all sections of the Author Contributions. The Author Contributions have since been corrected, and this version may be considered the authoritative version of record.